POLITECNICO DI TORINO
Repository ISTITUZIONALE

Multiscale developments of cellular Potts models

(Article begins on next page)

21 December 2024

MULTISCALE DEVELOPMENTS OF THE CELLULAR POTTS MODEL[*]

M. SCIANNA[†] AND L. PREZIOSI[†]

Abstract. Multiscale problems are ubiquitous and fundamental in all biological phenomena that emerge naturally from the complex interaction of processes which occur at various levels. A number of both discrete and continuous mathematical models and methods have been developed to address such an intricate network of organization. One of the most suitable individual cell-based model for this purpose is the well-known cellular Potts model (CPM). The CPM is a discrete, lattice-based, flexible technique that is able to accurately identify and describe the phenomenological mechanisms which are responsible for innumerable biological (and nonbiological) phenomena. In this work, we first give a brief overview of its biophysical basis and discuss its main limitations. We then propose some innovative extensions, focusing on ways of integrating the basic mesoscopic CPM with accurate continuous models of microscopic dynamics of individuals. The aim is to create a multiscale hybrid framework that is able to deal with the typical multilevel organization of biological development, where the behavior of the simulated individuals is realistically driven by their internal state. Our CPM extensions are then tested with sample applications that show a qualitative and quantitative agreement with experimental data. Finally, we conclude by discussing further possible developments of the method.

1. Introduction. All biological phenomena emerge from an intricate interaction of multiple levels of organization—the molecular scale, the cell, and the tissue; see Figure 1. These natural levels can approximately be connected to a microscopic, a mesoscopic, and a macroscopic scale, respectively. The microscopic scale refers to those processes that occur at the subcellular level, such as DNA synthesis and duplication, the activation of receptors, the transduction of chemical signals, and the diffusion of ions. The mesoscopic scale, on the other hand, can refer to cell-level phenomena, such as adhesive interaction between cells or between cells and fibers forming the extracullular matrix (ECM), cell duplication, and cell motion. Finally, the macroscopic scale corresponds to those processes that are typical of the multicellular level, such as population growth and dynamics.

However, the flow of information between these different spatial and temporal levels is often too complex to be studied with only *experimental techniques*; an increasing collaboration with *applied mathematics* is therefore necessary (for a comment refer to [59]). In fact, even though no hypothetically perfect single model (which is probably computationally unfeasible) can incorporate each and every aspect of all the processes involved in the considered phenomenon, a computational approach is able to simplify the biological problem and offers both a concise description of its essential features and the possibility of highlighting which experimental quantities are the most

≈ 10⁻⁵ m   ≈ 10⁻⁶ m   ≈ 10⁻⁷ m
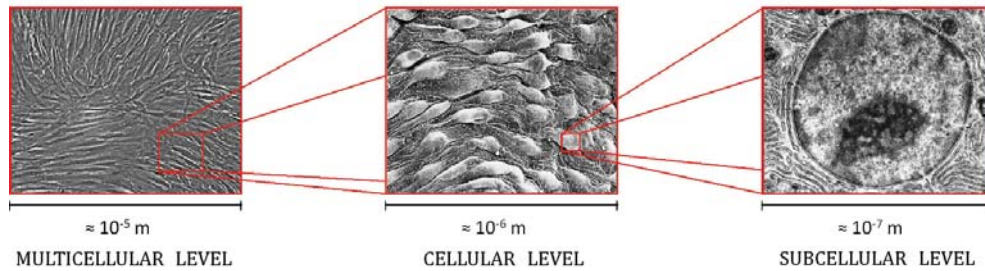MULTICELLULAR LEVEL   CELLULAR LEVEL   SUBCELLULAR LEVEL

FIG. 1. *Multiscale view of biological systems. A cell population consists of a huge number of cells. A zoom allows the identification of single polarized cells adhering to each other. A further zoom permits the identification and localization of intracellular elements, such as the nucleus, the Golgi Apparatus, and some mitochondria. Representative image kindly provided by the Department of Animal and Human Biology, Università degli Studi di Torino.*

relevant. It can also be used, in a predictive manner, to determine the consequences of experimental manipulations, and it can provide a useful guide for future experiments. Procedurally, a good approach is to build the simplest possible model, focused on a single scale and based on the minimal set of assumptions that are consistent with biological observations. After checking its validity with experimental results, it is then possible to gradually add more components and more levels of abstraction: this continuous feedback and feedforward between in silico and in vitro techniques can therefore in principle lead to a complete understanding of the complex multiscale mechanisms of the studied phenomenon.

Mathematical approaches to biological problems employ a wide range of techniques which depend on the particular spatio-temporal scale of interest; see Figure 2. However, most of them fall into two categories: *continuous* and *discrete* models.
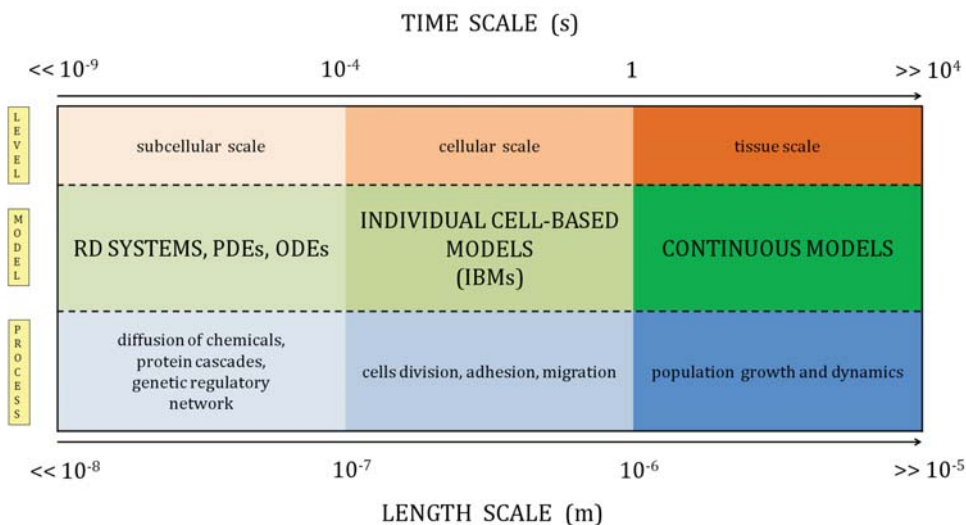

FIG. 2. *Hierarchies of biological length and temporal scales, and the corresponding modeling techniques.*

Continuous models approach biological phenomena in terms of variation of fields.

Characteristic of a macroscopic point of view, these methods represent populations of biological individuals as densities which evolve satisfying a set of balance laws or diffusion equations. However, continuous approaches overlook the behavior of single individuals and also fail to describe their pair interactions. Thus, when dealing with biological processes in which what occurs at the scale of the single elements is fundamental, continuous models may be unsatisfactory. In these cases, it is better to approach the biological problem adopting techniques that preserve the identity and the behavior of individual elements, e.g., *individual cell-based models* (IBMs); for comprehensive reviews see [1, 3, 47]. IBMs are discrete models that are focused on the cell level of abstraction. They represent biological individuals, with the typical length scale of a cell, as one or a set of discrete units, with rules that describe their movements and interactions. The morphology of the elements is restricted according to some underlying discretizations of the simulation domain, which can be either regular (such as square or cubic grids) or irregular (Voronoi tessellations). These approaches can be further classified into two categories: those in which each individual is correlated to a single spatial unit of the domain, and those in which each element can be constituted by a collection of spatial units. In comparison to continuous methods, IBMs can more naturally capture detailed biophysical properties, such as cell shape, geometry, and adhesion, and they are also able to handle local interactions between the simulated objects. In cell-based methods, the individuals behave according to a relatively small set of prescribed rules, which they execute depending on their type and the signals they receive from the neighbors and from the environment. In particular, these techniques are able to analyze the mechanisms by which the relatively simple behavior and interactions of individuals collectively direct macroscopic pattern formation and development, and, vice versa, to infer how phenomena that occur at the macroscopic level feed back to the phenomenology of single elements, as commented on in [59]. Moreover, cell-based models help to unravel how abnormal cell behavior can produce abnormal patterns. However, by approaching biological phenomena from a mesoscopic point of view, IBMs do not usually describe molecular-level processes and thus neglect the microscopic mechanisms that underlie individual phenomenology. Furthermore, since they are computationally expensive, they can only simulate several individuals at once.

In the last decade, we have witnessed an increasing integration of discrete and continuous techniques: the aim is to create modeling environments that are able to span a wide range of biological scales with a sufficient level of accuracy. Offering the advantages of both types of approaches, such *hybrid* methods usually use IBMs to represent the dynamics of single cell-level individuals and diffusion equations to describe the evolution of microscopic molecules; see, for example, [11, 25]. One of these approaches is the cellular Potts model (CPM), also called the Glazier–Graner–Hogeweg model, which was developed in [33, 35] and reviewed in [6, 34, 51].

As a generalization of the Ising model, the CPM is a grid-based, stochastic Monte Carlo method, based on an energy minimization philosophy, which drives the evolution of the simulated system. All CPM approaches represent the simulated environment on a lattice and define a list of objects. CPM objects can be both generalized cells and fields. Generalized cells are spatially extended, mesoscopic, cell-scale elements; they may correspond to unicellular organisms, cells, cell subcompartments, clusters of cells, ECM fibers, or portions of noncellular materials. The fields instead represent the spatio-temporal evolution of microscopic quantities, such as diffusive ions and molecules. The attributes of the discrete individuals, and the rules for their dynamics and interactions with fields, are described by an effective potential formalism and are

included in a system energy that is given by the *Hamiltonian*. This functional, which may include true energies (e.g., cell-cell adhesion) and terms that mimic energies (e.g., the response of a cell to a chemical gradient), describes the state of the system and drives all the lattice rearrangements with an algorithm of stochastic minimization (a modified Metropolis procedure which we will describe in detail in the next section). As long as a biological mechanism can be described with an energetic formalism, it can be included in the CPM framework. Thus the CPM is not for a specific type of biological problem but can be considered as a framework for model building. The new ideas, which are constantly emerging to extend it to describe new biological (and non-biological) phenomena, can in fact be automatically integrated with the whole body of prior work. Such flexibility, as well as a simplicity of implementation, make the CPM unusually rewarding to work with. The CPM method is becoming an increasingly common technique for the mathematical modeling of a wide range of biological phenomena, including avascular and vascular tumor growth [7, 75, 82, 91], gastrulation [27], skin pigmentation [65], yeast colony growth [92], stem cell differentiation [100], fruiting body formation of Dictyostelium discoideum [52], epidermal formation [77], hydra regeneration [63], retinal patterning [61], wound healing [50], biofilms [69], chick limb-bud growth [14, 15, 70], differential adhesion-driven cell rearrangement [34], cellular differentiation and growth of tissues, blood flow and thrombus development [96, 97, 98], angiogenesis [56, 57, 80], and cell scattering [78]. Figure 3 shows some of the innumerable applications of the CPM.

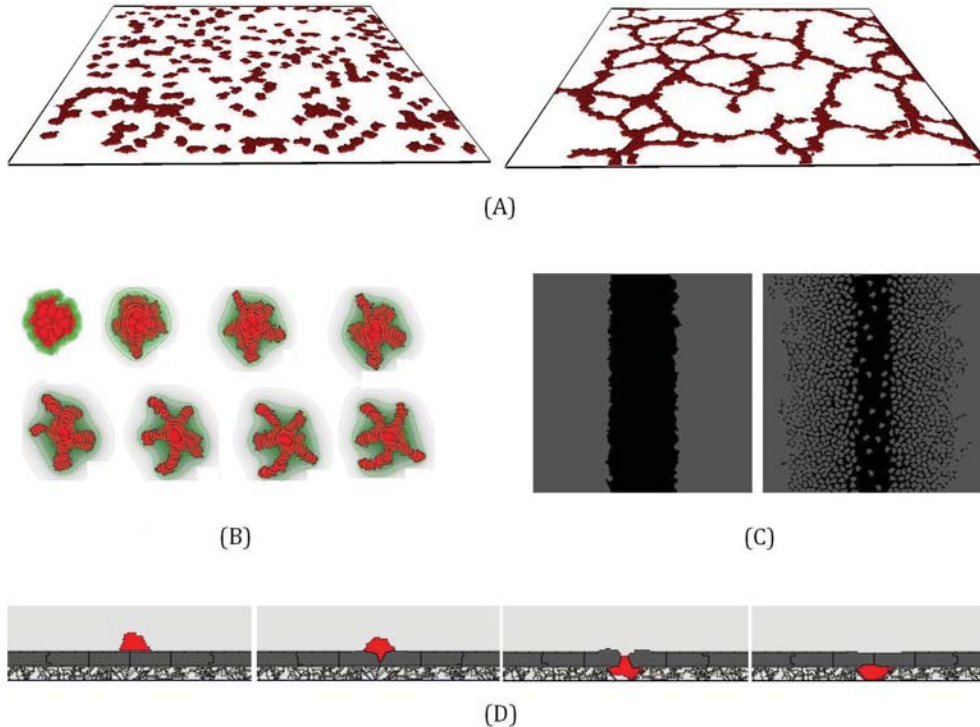
FIG. 3. *Different examples of CPM applications.* (A) *Calcium-dependent in vitro vasculogenesis* [80]. (B) *HGF-dependent scatter of hepatocyte cells* [78]. (C) *In vitro wound healing assay.* (D) *Ovarian cancer transmesothelial invasion* [32].

A brief review of the biophysical bases of the classical CPM is given in section 2 of this paper. In particular, we systematically examine and comment on some critical points that could be improved to make the model closer to reality. This preliminary discussion is the mandatory starting point from which to investigate and present some important developments of the method; our aim is in fact to provide useful guidance for the construction of more realistic and biologically accurate simulations. In particular, our developments, which are dealt with in detail in section 3, are focused on ways of describing the microscopic level, which is only roughly approached in the basic cell-level CPM. First, in section 3.1, we propose a more accurate representation of biological individuals, which can be realistically compartmentalized into reasonable subunits, such as cell nucleus, cytosol, plasmamembrane, and organelles. In section 3.2, we then give a plausible procedure to interface the basic CPM with accurate models of microscopic biochemical pathways, which modulate the mesoscopic properties of the simulated individuals (such as their motility, adhesive strength, and elasticity). In other words, the behavior of individuals can now continuously and realistically be driven by the evolution of their internal state and not defined only by a normally used qualitative set of a priori assumptions. In section 3.3, we propose alternative laws for the Boltzmann transition function, the core of the Metropolis algorithm, with special emphasis on the description of the motility of individuals. Throughout the text, we also illustrate some relevant test applications, showing how our approach can improve the accuracy of real multiscale simulations to a great extent. Our extended CPM can in fact be easily adapted to different biological contexts of interest, while maintaining good qualitative and quantitative agreement with experimental evidence. In the last part of the work, after a useful discussion on the computational implementations of the method given in section 5, we draw conclusions and briefly comment on other possible developments for further improvements of the CPM.

2. Basic CPM. All CPM approaches include a list of objects, a description of their interactions, and rules for their dynamics. The CPM domains are d-dimensional lattices $\Omega \subseteq \mathbb{R}^d$, where $d = 1, 2, 3$. The term lattice defines a regular repeated graph, formed by identical d-dimensional grid sites $\mathbf{x} \in \mathbb{R}^d$, and characterized by periodic or fixed boundary conditions in each direction. The volumetric extension of Ω is equal to the total number of its sites, which therefore represents the basic unit of length of the system. Each site $\mathbf{x} \in \Omega$ is uniquely identified by its location and is labeled by an integer number, $\sigma(\mathbf{x}) \in \mathbb{N}$, where σ can be interpreted as a degenerate spin value coming from the original Ising approach [19, 43, 71]; see Figure 4(A). As classically adopted in CPM models, a neighboring site of $\mathbf{x}$ is denoted by $\mathbf{x}'$ and its overall neighborhood by $\Omega'_{\mathbf{x}}$, i.e., $\Omega'_{\mathbf{x}} = \{\mathbf{x}' \in \Omega : \mathbf{x}' \text{ is a neighbor of } \mathbf{x}\}$.

Objects in the CPM are either *discrete* or *continuous*. Discrete objects are finite, spatially extended lattice subdomains of contiguous sites denoted with the same spin σ. They are therefore undifferentiated *functional units* which, in basic CPMs, represent single biological elements with the typical mesoscopic length scale of a cell. Examples are bacteria, unicellular organisms, single cells, ECM fibers, or other substrates; see Figure 4(B–C). Trivially, a collection of N discrete individuals is defined by N integers, $\sigma = 1, 2, \ldots, N$. The borders between sites with different spins, which are thus shared between a couple of objects, define their membranes. Each unit σ has a set of attributes (both geometrical, such as volume and surface, and biophysical, such as velocity and elasticity) and an associated type $\tau(\sigma)$ (e.g., endothelial cell, fibroblast, or ECM fiber). Mesoscopic, cell-level objects rearrange their boundaries to realistically reproduce shape changes and motion. Moreover, they can grow, die, du-

(A)

50 µm   (B)   50 µm

5 nm   (C)   100 nm
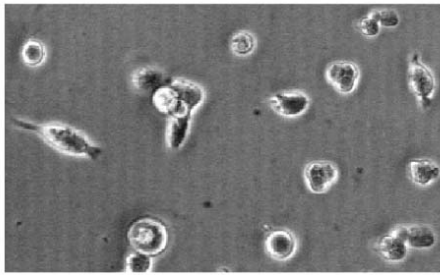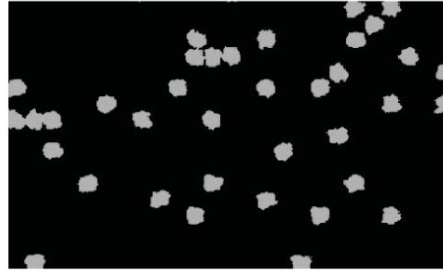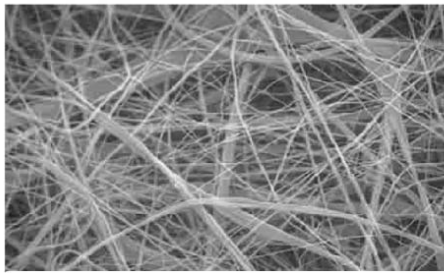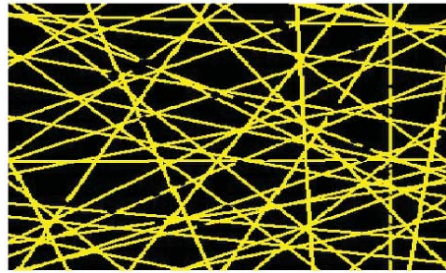
Fig. 4. (A) *Typical 2D rectangular CPM lattice. The integer numbers (σ) identify single discrete objects. The individual $\sigma = 5$ and $\sigma = 6$ are of the same type τ and are identified by the same color. (B) Population of experimental cells (image courtesy of Prof. Luca Munaron and of the Department of Animal and Human Biology, Università degli Studi di Torino) and virtual cells. (C) Anisotropic fibers of collagen I in the reality (representative image kindly provided by the Department of Animal and Human Biology, Università degli Studi di Torino) and in a sample simulation. Note the different length scale between the in vitro and in silico images.*

plicate (and the daughter objects typically inherit some the properties of their parent [39, 64, 70]), and carry a set of possible rules for transitions between types (a cell type map (CTM) [18]). Sometimes, we use the notation σ' to identify a discrete object neighbor of σ.

Continuous objects, or *fields*, represent the spatio-temporal evolution of micro-

scopic entities, which are described as variable concentrations. They may reside within the discrete objects (as DNA, RNA, cytosolic ions, and proteins) or in the external environment (as growth factors, matrix proteins, and matrix metallo-proteinases). The continuous equations that describe the variation of the microscopic quantities are numerically solved on grids that exactly match the domain Ω and that are discretized at the same resolution.

Interactions between discrete cell-level objects and continuous molecular-level objects (for example, cell absorption and secretion of chemical diffusants) are characterized either by auxiliary equations [37, 53] or by specific terms in the field equations themselves [7, 80]. This coupling between the dynamics of microscopic and mesoscopic objects constitutes a typical hybrid modeling approach. The motion of the discrete objects may cause continuous fields to evolve into subdomains with moving boundaries.

Obviously, each CPM application needs the specification of the initial condition of the lattice, i.e., the initial spatial configuration of all the objects.

The CPM core principle consists of an iterative stochastic minimization of a system free energy, which is described by the *Hamiltonian functional H*, that will be defined in detail below. Simulated objects in fact rearrange and evolve to gradually reduce such a pattern energy looking for a global minimum, rather than toward a configuration in which multiple local minima coexist. Since the energy gradient is not completely smooth, on its way to global minimization, the system has to move through transient states, which are characterized by higher energies than the previous configurations. This energy minimization philosophy is implemented by adopting a modified version of the classical Metropolis algorithm for Monte Carlo–Boltzmann thermodynamics [35, 60]. It evolves in time using repeated probabilistic updates of the site identification spins. Procedurally, at each simulation time step, t, a lattice site $\mathbf{x}$, belonging to an object interface, is randomly selected (*source voxel*) and proposed to copy its spin $\sigma(\mathbf{x})$ into an arbitrary unlike neighbor $\mathbf{x}'$ (*target voxel*). The proposed change in the lattice configuration (also called *spin flip*) is accepted with a classical *Boltzmann transitional probability*, which is a relic of the CPM descent from statistical physics [71]:

$$(2.1) \qquad P(\sigma(\mathbf{x}) \to \sigma(\mathbf{x}'))(t) = \begin{cases} e^{-\Delta H|_{\sigma(\mathbf{x}) \to \sigma(\mathbf{x}')}/T}, & \Delta H|_{\sigma(\mathbf{x}) \to \sigma(\mathbf{x}')} > 0 \,, \\ \\ 1, & \Delta H|_{\sigma(\mathbf{x}) \to \sigma(\mathbf{x}')} \leq 0 \,, \end{cases}$$

where

$$(2.2) \qquad \Delta H|_{\sigma(\mathbf{x}) \to \sigma(\mathbf{x}')} = H_{after\ spin\ flip} - H_{before\ spin\ flip}$$

is the net variation in the total energy of the system as a consequence of the spin update and $T \in \mathbb{R}^+$ is a Boltzmann temperature, which does not reflect any conventional thermal temperature, but in basic CPMs broadly correlates to an overall *system motility*. T is measured in units of energy. In one of our recent papers [32] such a motility is allowed to depend on the object type ($T = T(\tau)$); however, it is also possible to relate it to each single unit, $T = T(\sigma)$. This aspect is described in more detail in sections 3.2 and 3.3. The nomenclature of T originates from the fact that membrane agitation rates in biological individuals play an analogous role to real temperatures in ordinary thermodynamics [62]. From a statistical point of view, T represents the likelihood of the energetic unfavorable changes in lattice configurations, since it determines the rate of their acceptance. For very small values, the system

evolution is almost deterministic, and it can be trapped in local minima. For very large T all moves are accepted, and the simulated objects are characterized by a biased random walk in the absence of potential barriers. Their motility, in fact, overcomes the constraints set by the local environment, since $\Delta H|_{\sigma(\mathbf{x}) \to \sigma(\mathbf{x}')}/T \to 0$ for all the proposed displacements of its membrane sites. After the discrete object σ has evolved through a spin flip, both equations that describe the variation of continuous fields and the attributes of all the objects are rederived on the basis of new lattice configuration. The basic step of the Metropolis algorithm is then iterated until the end of the simulation time or until the whole system reaches an energetic global minimum, if it exists.

The unit of time of all CPM approaches is the *Monte Carlo step* (MCS). An MCS corresponds to a fixed number of trial lattice updates, which usually consists of a multiple of the total number of sites of Ω (i.e., 1 MCS $= k \cdot$ Volume$_\Omega$) and which has to be translated into the actual unit of time (i.e., seconds, hours, or days).

The discrete *effective energy* of the system, given by the Hamiltonian H, may contain a variable number of terms, which can be grouped as

$$(2.3) \qquad H(t) = H_{adhesion}(t) + H_{constraint}(t) + H_{force}(t).$$

$H_{adhesion}$ describes the adhesive/repulsive interfacial energy between all the couples of discrete objects that interact across their common membrane. $H_{adhesion}$ is based on Steinberg's *differential adhesion hypothesis* (DAH) [35, 84, 85]. The DAH proposes that individuals in the same aggregate adhere to each other with different strengths, according to their type. Such a hierarchy of contact forces is one of the main driving mechanisms behind of the evolution of biological systems, whose final organization maximizes the overall strength of interface interactions (or, in other words, minimizes the overall adhesion energy). However, the DAH says nothing about the dynamics of moving objects: differential adhesion itself, in fact, helps only to select the most favorable configuration among the different possibilities that have been explored. Evidence supporting DAH has been observed in a wide array of biological systems; for example, it successfully explains how cellular adhesive properties can operate to determine tissue reorganization during cell sorting [4, 34, 35]. The typical formulation of DAH-derived $H_{adhesion}$ is

$$
\begin{aligned}
H_{adhesion}(t) &= \sum_{\mathbf{x} \in \Omega, \mathbf{x}' \in \Omega'_{\mathbf{x}}} J_{\tau(\sigma(\mathbf{x})),\tau(\sigma(\mathbf{x}'))}(t)[1 - \delta_{\sigma(\mathbf{x}),\sigma(\mathbf{x}')}(t)] \\
&= \sum_{\substack{\mathbf{x} \in \Omega, \mathbf{x}' \in \Omega'_{\mathbf{x}} \\ \sigma(\mathbf{x}) \neq \sigma(\mathbf{x}')}} J_{\tau(\sigma(\mathbf{x})),\tau(\sigma(\mathbf{x}'))}(t),
\end{aligned}
$$

(2.4)

where $\Omega'_{\mathbf{x}}$ is, as seen, the neighborhood of site $\mathbf{x}$, and the Kronecker delta is $\delta_{m,n} = \{1, m = n; 0, m \neq n\}$, ensuring that only links between different objects (i.e., $\sigma(\mathbf{x}) \neq \sigma(\mathbf{x}')$) contribute to the overall contact energy. The coefficients $J_{\tau(\sigma(\mathbf{x})),\tau(\sigma(\mathbf{x}'))} \in \mathbb{R}$ are the binding forces per unit area, the first type of the so-called Potts parameters, and are obviously symmetric. In basic CPMs, they depend only on the type of discrete objects that are in contact (i.e., $\tau(\sigma(\mathbf{x}))$ and $\tau(\sigma(\mathbf{x}'))$ in (2.4)), as they are not a characteristic of each single unit; see, for example, [58, 62, 75, 76]. Moreover, they are uniformly distributed over the whole surface of the discrete objects, neglecting microscopic inhomogeneities, such as a clusterization or a different strength of adhesion in well-localized parts of their membranes. This issue will be discussed in more detail in

section 3.2, as the model will be extended in this respect. In the case of cells, such contact strengths give a qualitative measure of the expression of adhesion molecules in the individuals on either side of the common border, whose activity defines their binding properties. In particular, at least two classes of J can be identified—those relative to the adhesion between cells and extracellular material (and thus modeling the activity of cell-matrix adhesion molecules, such as integrins), and those that mediate the adhesion between cells of either the same or different populations (and thus related to the expression of cell-cell adhesion molecules, such as cadherins). A surface contact force can also be defined with an external undifferentiated medium (for example, culture medium, air, or generic substrate), but it is biologically meaningless.

The term $H_{constraint}$, whose use also comes from the physics of classical mechanics, sums the energetic components that describe the object attributes. They are written as energetic penalties which increase as the objects deviate from a designed state, in a characteristic elastic form,

$$(2.5) \qquad H_{constraint}(t) = \sum_{\sigma} \sum_{i-constraint} \lambda_\sigma^i(t) \left[a_\sigma^i(t) - A_\sigma^i(t) \right]^2,$$

where $a_\sigma^i(t)$ is the actual value of the i-attribute of individual σ, and $A_\sigma^i(t)$ is its target value, that usually characterizes an object type and that can vary in time. $\lambda_\sigma^i \in \mathbb{R}^+$ are spring moduli, other Potts parameters, which determine the weight of the relative energetic constraint and thus the importance of the relative attribute. Low values of λ_σ^i in fact allow the discrete unit σ to deviate more from the configuration that satisfies the constraint. Since the energetic contributions given in (2.5) decrease smoothly to a minimum when the attributes are satisfied, the modified Metropolis algorithm automatically drives any configuration toward one that satisfies the constraints. Obviously, the simulated system is not able to exactly satisfy all the constraints of all the objects σ at any given time t, since multiple attributes may be in conflict; this leads to stochastic lattice configurations which fluctuate around the equilibrium condition. Among others, the energetic components relative to geometrical attributes of discrete objects, such as their volume and surface, are of particular relevance. These components depend on the actual measures of each mesoscopic element, $a_\sigma^{volume}(t)$ and $a_\sigma^{surface}(t)$, as well as on the same quantities in the relaxed/undeformed state $A_\sigma^{volume}(t)$ and $A_\sigma^{surface}(t)$. In particular, λ_σ^{volume} regulates the conservation of mass of the discrete objects, and encodes all the bulk effects: moreover, their growth can be realistically included by assuming that $A_\sigma^{volume}(t)$ increases during the simulation [14, 70]. $\lambda_\sigma^{surface}$ instead represents the inverse compressibility of σ, the ease with which it can change its shape. If $\lambda_\sigma^{surface}$ is very large, σ has a negligible elasticity, and its membrane is tight. In particular, for $\lambda_\sigma^{volume}, \lambda_\sigma^{surface} \to \infty$, σ behaves as a rigid body. In the case of cells, λ_σ^{volume} and $\lambda_\sigma^{surface}$ regulate, respectively, the growth and the change of shape due to active reorganizations of the actin cytoskeleton triggered by both internal stimuli (such as small G-protein activity), or external stimuli (such as ECM contact guidance).

Attribute constraints, and the relative energetic penalties, can also regulate interactions between objects. Their form is analogous to (2.5):

$$(2.6) \qquad H_{constraint}(t) = \sum_{\sigma,\sigma'} \sum_{j-constraint} \lambda_{\sigma,\sigma'}^j(t) \left[a_{\sigma,\sigma'}^j(t) - A_{\sigma,\sigma'}^j(t) \right]^2.$$

A typical example is a linear spring connecting the center of mass of a pair of cells (σ, σ'). In this case, $A_{\sigma,\sigma'}^j$ represents the equilibrium length of the connection, and

$a_{\sigma,\sigma'}^j$ is the actual distance between the center of mass of the two neighboring cells. Such a constraint is useful, for instance, when representing tight junctions between endothelial cells in a mature capillary which maintain the integrity of the vessel [82].

The last term in (2.3) includes the energetic counterparts of the forces (both effective and generalized) that act on the simulated individuals. All of these are described with the same architecture [22]:

$$(2.7) \qquad H_{force}(t) = - \sum_{\mathbf{x} \in \sigma} \sum_{k-force} \mu_\sigma^k(t) \, \mathbf{F}^k(t) \cdot \mathbf{r_x},$$

where $\mathbf{r_x} = (i_\mathbf{x}, j_\mathbf{x}, k_\mathbf{x})^T$ is the position vector of lattice site $\mathbf{x}$, which is the application point of force $\mathbf{F}^k$, and μ_σ^k is the relative Potts parameter, which measures the effective strength of the force on object σ. The most diffused examples in CPM applications are the forces that are exerted by extracellular chemical substances (which are continuous CPM objects) on a population of cells (which are, as seen, discrete objects):

$$(2.8) \qquad H_{force}^{chemical}(t) = - \sum_\sigma \sum_{\mathbf{x} \in \sigma} \mu_\sigma(t) c(\mathbf{x}, t),$$

where $c(\mathbf{x}, t)$ is the concentration of the chemical sensed by cell site $\mathbf{x}$ (which can be modeled as the local chemical concentration in site $\mathbf{x}$ itself [41, 56] or in its neighborhood [79, 80]), and the Potts coefficient μ_σ is, in this case, an effective chemical potential of cell σ. Moreover, the net energy difference caused by such a chemical force is

$$(2.9) \qquad \Delta H_{force}^{chemical}\big|_{\sigma(\mathbf{x}) \to \sigma(\mathbf{x}')} = \mu_\sigma[c(\mathbf{x}, t) - c(\mathbf{x}', t)],$$

where $\mathbf{x}$, which, as usual, belongs to the border of σ, and $\mathbf{x}'$ are the two neighboring lattice sites randomly selected during the trial update at time t [76]. If μ_σ is a constant, σ has a linear chemical sensitivity. In particular, $\mu_\sigma > 0$ yields to its motion up the gradient of c (which is thus a *chemoattractant*, and the relative force is called *chemotaxis*), while $\mu_\sigma < 0$ yields to its motion in the opposite direction (and c is a *chemorepellent*). Moreover, if c is a nondiffusive fixed substrate, (2.8) is a representation of a haptotactic force, as in [49, 91].

3. Developments. Basic CPM approaches work surprisingly well in the modeling of a wide range of biological processes. In particular, they can provide important new insights into the principles of multicellular (tissutal) patterning in a number of phenomena, as they are able to analyze their driving mechanisms; see, for example, [37, 51, 70]. Moreover, CPM applications are a way of comparing the outcomes of different and equally plausible scenarios, providing a predictive value as well. Authors can in fact analyze the system's response to a range of experimental perturbations, as shown in [49, 59, 80, 82].

The first advantage of the CPM compared to alternative cell-based modeling approaches that represent biological individuals as point particles or fixed-sized spheres or ellipsoids (for examples see [3]) is that it differentiates between bound and unbound regions of their membranes. Moreover, morphologies and changes of shape of discrete elements are easily and realistically implemented. The key benefits of the CPM energetic formalism are its simplicity and extensibility. Almost any biological mechanism can in fact be included in the model, simply by adding an appropriate generalized potential term in the Hamiltonian H, as suggested in the main reviews

of the method [6, 33]. It is therefore possible to easily comprehend the importance of each mechanism involved in the simulated phenomenon by only altering the relative Potts parameter so that the other terms in the Hamiltonian scale accordingly. In particular, by equating all the other terms to zero, it is possible to understand whether such a mechanism is individually capable of producing the process of interest or whether it requires cooperative processes.

However, most CPM approaches suffer from some limitations. First, the reproduction of biological entities is improbable, since they are usually represented by single discrete objects, which are isotropic and formed by equivalent and undifferentiated sites. This representation provides a useful level of abstraction but also hides relevant inhomogeneous properties that characterize all biological individuals. For example, in the case of simulated cells reproduced by a single functional unit, the cytoskeleton and the plasmamembrane do not have an independent existence on one hand, while, on the other, the nuclear envelope is not defined. Moreover, while certain model quantities, such as energy or temperature, have unambiguous meanings, most Potts parameters do not have a direct correspondence with biophysical measurable quantities; see also [59] for a comment. This is a crucial drawback for a good quantitative comparison between in silico and in vitro results and thus for a predictive value of CPM applications. Additionally, these constraint weights, which modulate the dynamic behavior of the simulated individuals, are generally static over the whole simulation or have unrealistic variations. This situation in not plausible since real biological elements continuously change their biophysical and biomechanical properties as a consequence of continuous internal and external stimuli. These considerations lead to one of the main criticisms of CPM approaches: most simulated phenomena emerge from quite strong a priori assumptions that are derived from experimental observation; see again [59]. In particular, the behavior of the simulated individuals is imposed by qualitative rules (such as the energetic constraints regulated by fixed parameters) that do not easily adapt during the evolution of the system. Furthermore, by treating simulated individuals with only this cell-level phenomenologic approach, most CPM applications do not consider (or, in some cases, only approximately describe) the molecular scale of the biological organisms, as explained in [33]. In fact, basic CPMs neglect the continuous flow of information between the microscopic and the mesoscopic scales, which, as seen in the introduction, is fundamental for developmental biology. Finally, all the objects belonging to a given type (τ) are usually constrained to feature the same biophysical properties, such as the target states of most attributes or the adhesive strength, despite their individuality.

In the next sections, we propose some extensions for CPM applications in order to overcome the above-cited limitations and to improve the biological realism of the method.

3.1. Compartmentalization approach. As we have seen, most existing CPMs generally treat biological individuals as undifferentiated discrete objects, i.e., single functional units identified by a common spin σ. Different spin states therefore represent different simulated entities. However, biological elements are composed of different parts (such as the nucleus or the cytosol in a eukaryotic cell or the microcompartments in bacteria) which play a fundamental and unique role in the development of the organism. Moreover, each of these parts is characterized by particular and well-defined biophysical, biochemical, and biomechanical properties.

The simplest and most realistic way of reproducing such complex morphologies is to introduce a *compartmentalization* technique. According to this approach, a collec-

SYMBOL	BASIC CPM	EXAMPLE	COMPARTMENTALIZED CPM	EXAMPLE
σ	object → single individual	$\sigma = 1,2$	object → individual compartment	$\sigma = 1,2,3,4,5,6,7,8,9,10$ $\eta = \quad 1 \quad , \quad 2$
η			cluster → single individual	
τ	object type → individual type	$\tau(\sigma=1)$=endothelial cell $\tau(\sigma=2)$=fibroblast	object type → compartment type	$\tau(\sigma=1,5)$=nucleus $\tau(\sigma=2,6)$=cytosol $\tau(\sigma=3,7)$=PM $\tau(\sigma=4,8)$=Golgi $\tau(\sigma=9,10)$=medium
θ			cluster type → individual type	$\theta(\eta=1)$=endothelial cell $\theta(\eta=2)$=fibroblast

(A)

(B)

FIG. 5. (A) *Table of the symbolism used in both the standard CPM and in the compartmentalized extension, with appropriate examples.* (B) *Bidimensional square CPM domain representing the elements defined in the compartmentalized example in the above table. The bold borders indicate their external membranes and the light borders their internal ones.* $\eta = 1, 2$ *are compartmentalized individuals, each of which is formed by four units, while* $\sigma = 9, 10$ *are standard, noncompartmentalized individuals.*

tion of standard CPM objects can be clustered to form a compartmentalized element, which can better reproduce a real biological individual. In other words, if in the basic CPM a single discrete object represented an entire individual, it now represents one of its compartments. Technically, with the new procedure, the discrete units, identified, as usual, with their spin σ, share an additional attribute, a cluster id $\eta(\sigma) \in \mathbb{N}$, which defines the compartmentalized individual they belong to. Obviously, discrete units without η are not part of a compartmentalized entity, but represent, on their own, an entire element (as in the basic CPMs). Apart from the type already defined for the discrete units, $\tau(\sigma)$, we can now introduce a type for the entire clusters, $\theta(\eta)$; see Figure 5(A). The compartmentalized individuals η of the same family θ are formed by the same number and type of units σ. The borders between subunits belonging to the same individual represent its internal membranes. Referring to Figure 5 as an example, we see that the discrete objects $\sigma = 1, 2, 3, 4$ are clustered in individual

$\eta = 1$, which represents an endothelial cell, while objects $\sigma = 5, 6, 7, 8$ form individual $\eta = 2$, which represents a fibroblast. Moreover, units $\sigma = 9$ and 10 represent entire standard noncompartmentalized entities.

This new representation of individuals requires a redefinition of the characteristic quantities of the CPM. First, it is necessary to differentiate the contributions of $H_{adhesion}$ due either to the contact between discrete units belonging to the same element, or to the contact between discrete units belonging to different elements, which, from a biological point of view, are of different nature. Hence, we distinguish between external and internal contact adhesions:

$$(3.1) \qquad H_{adhesion}(t) = H_{adhesion}^{int}(t) + H_{adhesion}^{ext}(t).$$

In particular, $H_{adhesion}^{int}$ models generalized contact forces between couples of objects that belong to the same individual, e.g., the nucleus and the cytosol in a cell:

$$
\begin{aligned}
H_{adhesion}^{int}(t) &= \sum_{\mathbf{x}\in\Omega, \mathbf{x}'\in\Omega'_{\mathbf{x}}} J_{\tau(\sigma(\mathbf{x})),\tau(\sigma(\mathbf{x}'))}^{int}(t)\delta_{\eta(\sigma(\mathbf{x})),\eta(\sigma(\mathbf{x}'))}(t)[1 - \delta_{\sigma(\mathbf{x}),\sigma(\mathbf{x}')}(t)] \\
(3.2) \qquad &= \sum_{\substack{\mathbf{x}\in\Omega, \mathbf{x}'\in\Omega'_{\mathbf{x}} \\ \eta(\sigma(\mathbf{x}))=\eta(\sigma(\mathbf{x}')) \\ \sigma(\mathbf{x})\neq\sigma(\mathbf{x}')}} J_{\tau(\sigma(\mathbf{x})),\tau(\sigma(\mathbf{x}'))}^{int}(t).
\end{aligned}
$$

The form of (3.2) is analogous to that of (2.4), as well as the Kronecker deltas. $J_{\tau(\sigma(\mathbf{x})),\tau(\sigma(\mathbf{x}'))}^{int} \in \mathbb{R}^-$ account for high contact tensions (we refer the reader to [66] for comments), which prevent single individuals from splitting.

$H_{adhesion}^{ext}$ is formed instead by the effective adhesion energies between different compartmentalized individuals, which interact with their external membranes:

$$
\begin{aligned}
H_{adhesion}^{ext}(t) &= \sum_{\mathbf{x}\in\Omega, \mathbf{x}'\in\Omega'_{\mathbf{x}}} J_{\tau(\sigma(\mathbf{x})),\tau(\sigma(\mathbf{x}'))}^{ext}(t)[1 - \delta_{\eta(\sigma(\mathbf{x})),\eta(\sigma(\mathbf{x}'))}(t)][1 - \delta_{\sigma(\mathbf{x}),\sigma(\mathbf{x}')}(t)] \\
(3.3) \qquad &= \sum_{\substack{\mathbf{x}\in\Omega, \mathbf{x}'\in\Omega'_{\mathbf{x}} \\ \eta(\sigma(\mathbf{x}))\neq\eta(\sigma(\mathbf{x}')) \\ \sigma(\mathbf{x})\neq\sigma(\mathbf{x}')}} J_{\tau(\sigma(\mathbf{x})),\tau(\sigma(\mathbf{x}'))}^{ext}(t).
\end{aligned}
$$

The strengths $J_{\tau(\sigma(\mathbf{x})),\tau(\sigma(\mathbf{x}'))}^{ext} \in \mathbb{R}^+$ depend, as usual, on the type of unit σ in contact. As a simple extension of the basic CPM, they may also depend on the types of the respective interacting clusters (i.e., on $\theta(\eta(\sigma(\mathbf{x})))$ and $\theta(\eta(\sigma(\mathbf{x}'))))$. However, in the present form, the J^{ext}'s remain spatially homogeneous throughout the object membranes and do not depend on the single units in contact. These issues will be addressed in the following section. It is worth noticing that, if the objects in contact represent standard noncompartmentalized individuals, then the relative energetic contributions are in the classical form of (2.4).

The compartmentalized approach requires us then to define the attributes, and the relative energetic contributions, of all the units and those that regulate their mutual interactions. A straightforward generalization of (2.5) and (2.6) results in

$$(3.4) \qquad H_{constraint}(t) = \sum_{\eta,\sigma,i-constraint} \lambda_{\eta,\sigma}^{i}(t)\left[a_{\eta,\sigma}^{i}(t) - A_{\eta,\sigma}^{i}(t)\right]^2;$$

$$(3.5)$$

$$H_{constraint}(t) = \sum_{(\eta,\eta'),(\sigma,\sigma'),j-constr} \lambda_{(\eta,\eta'),(\sigma,\sigma')}^{j}(t)\left[a_{(\eta,\eta'),(\sigma,\sigma')}^{j}(t) - A_{(\eta,\eta'),(\sigma,\sigma')}^{j}(t)\right]^2,$$

where $a^i_{\eta,\sigma}$ and $a^j_{(\eta,\eta'),(\sigma,\sigma')}$ are the actual values of the attributes, $A^i_{\eta,\sigma}$ and $A^i_{(\eta,\eta'),(\sigma,\sigma')}$ are their target values, and $\lambda^i_{\eta,\sigma}$ and $\lambda^i_{(\eta,\eta'),(\sigma,\sigma')} \in \mathbb{R}^+$ are the relative Potts parameters. However, we prefer to define the constraint contributions to the Hamiltonian as

$$(3.6) \qquad H_{constraint}(t) = \sum_{\eta,\sigma,i-constraint} \lambda^i_{\eta,\sigma}(t)(t) \left| \frac{a^i_{\eta,\sigma}(t) - A^i_{\eta,\sigma}(t)}{a^i_{\eta,\sigma}(t)} \right|^p ,$$

(3.7)

$$H_{constraint}(t) = \sum_{(\eta,\eta'),(\sigma,\sigma'),j-constr} \lambda^j_{(\eta,\eta'),(\sigma,\sigma')}(t) \left| \frac{a^j_{(\eta,\eta'),(\sigma,\sigma')}(t) - A^j_{(\eta,\eta'),(\sigma,\sigma')}(t)}{a^j_{(\eta,\eta'),(\sigma,\sigma')}(t)} \right|^p ,$$

with $p \in \mathbb{R}^+$. These latter forms allow us to have finite energetic contributions as well as a blow-up in the case of $a^i_{\eta,\sigma}, a^j_{(\eta,\eta'),(\sigma,\sigma')} \to 0$. This means that, for instance, an infinite energy is needed by a discrete unit to achieve a vanishing value of one of its constraints, e.g., shrinking a cell to a point. Moreover, in this way, all the components of $H_{constraint}$ are nondimensional, and thus all the relative Potts coefficients are coherently scaled to units of energy.

Finally, we characterize the forces acting on each object with

$$(3.8) \qquad H_{force}(t) = -\sum_{\mathbf{x} \in \sigma} \sum_{k-force} \mu^k_{\eta,\sigma}(t) \, \mathbf{F}^k(t) \cdot \mathbf{r_x}(t),$$

where $\mu^k_{\eta,\sigma}$ is the Potts coefficient that measures the effective strength of the force $\mathbf{F}^k$ sensed by the unit σ of the individual η.

Although each simulated element can in principle be compartmentalized in a variety of ways (for example, along symmetry planes, or in a fixed number of equivalent and undifferentiated subunits), a biologically plausible compartmentalization is preferable as the subunits, and the relative attributes, assume experimentally relevant meanings. An accurate and realistic representation of individuals is in fact also mandatory for a detailed description of their internal, microscopic mechanisms, whose introduction into the CPM method can be considered a further improvement, which will be introduced in the next section. All biochemical and biomechanical processes are in fact strongly localized within biological organisms and are characteristic of well-defined subcompartments. Moreover, the compartmentalized approach is clearly flexible, since it allows the level of detail to be tuned by only increasing or decreasing the number of units that form the clustered individual, or the number of lattice sites per functional unit. However, it is obviously computationally expensive, and often such a level of detail is neither required nor relevant for a good simulation of a number of biological processes. The optimal strategy depends on the phenomenon of interest, which therefore requires a preliminary analysis.

The compartmentalization technique is not entirely new in the CPM; it was in fact first introduced in [83], where the authors have subdivided a Myxococcus Xanthus into strings of subcellular domains in order to give the bacterium a particular geometry and to control its overall length. Moreover, in [53] a keratocyte has been represented with a set of undifferentiated hexagonal subunits, which have allowed us to reproduce its polarization during motion. Although these approaches are correct, the fact that the proposed subcellular compartments do not have an immediate or direct correspondence with real subcellular elements has limited the practicality and the
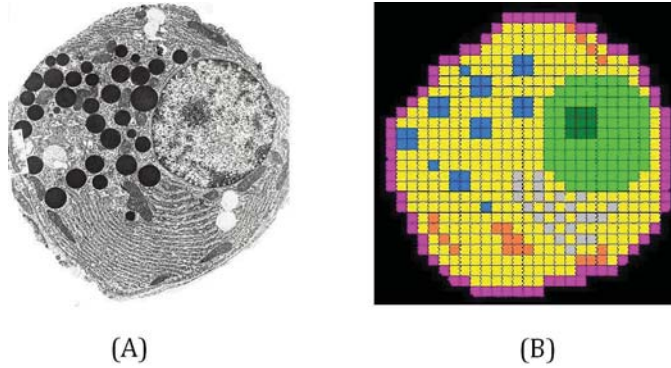
(A)   (B)

FIG. 6. *Comparison between a cell section of* (A) *electron micrograph and* (B) *compartmentalized CPM cells. In both cases, it is straightforward to identify the nucleus, the nucleolus, the plasmamembrane, the Golgi Apparatus, some mitochondria, and some secretory granules.*

usefulness of the relative models. As explained above, to the best of our knowledge, the most accurate way of realistically reproducing different and extremely complex cell morphologies is to compartmentalize them according to the compartmentalization suggested in nature, and thus to explicitly represent the plasmamembrane (PM), the cytosolic region, the nucleus, and other intracellular organelles (e.g., mitochondria, ribosomes, Golgi apparatus, and secretory granules; see Figure 6). This approach also allows us to accurately model most of the main intracellular phenomena. For instance, the introduction of an explicit PM permits us to define the activity of surface receptors, as well as to better describe the cell adhesive properties, i.e., to simulate the diffusion of adhesion molecules from the cell cytosol or their clusterization within particular regions. Moreover, it is possible to reproduce the active and continuous reorganization of the cytoskeleton, which provides the mechanical support for cells and mediates their coordinated and directed movements, in response to mechanical tensions and stresses from the local environment or to internal biochemical signals. The explicit representation of the cell nucleus would instead be mandatory to model genetic mechanisms such as DNA duplication, RNA synthesis, and diffusion.

3.1.1. An example: Endothelial cell chemotactic migration. As a simple test simulation, we model the chemotactic migration of a single endothelial cell (EC), placed on one side of a three-dimensional CPM domain Ω of $600 \times 200 \times 80$ sites, and stimulated by an exogenous vasculuar endothelial growth factor (VEGF) source, which is located on the opposite side. In this case, one lattice site is set to correspond to 0.125 μm^3, while one Monte Carlo step is set to 10 s. The cell, which initially is a hemisphere, is differentiated into three compartments: a central spheric nucleus ($\sigma = 1$, $\tau(\sigma) = N$), the surrounding cytosol ($\sigma = 2$, $\tau(\sigma) = C$), and the PM ($\sigma = 3$, $\tau(\sigma) = M$), which encloses the entire cell; see Figure 7(A). The cell cluster id of $\{\sigma : \sigma = 1, 2, 3\}$ is $\eta = 1$, of type $\theta(\eta) = E$. We further define a special generalized object ($\sigma = 0$, $\tau(\sigma) = Q$) which represents the extracellular medium, and which is assumed to be homogeneously distributed throughout the simulation domain, forming no large-scale structures and thus without volume or surface attributes. The extracellular substrate is also static and passive: cells can change it only by occupying sites which, once abandoned, return to a matrix state. The Hamiltonian H is formed by the geometrical attributes of the cell units, by the generalized adhesion terms, and by the
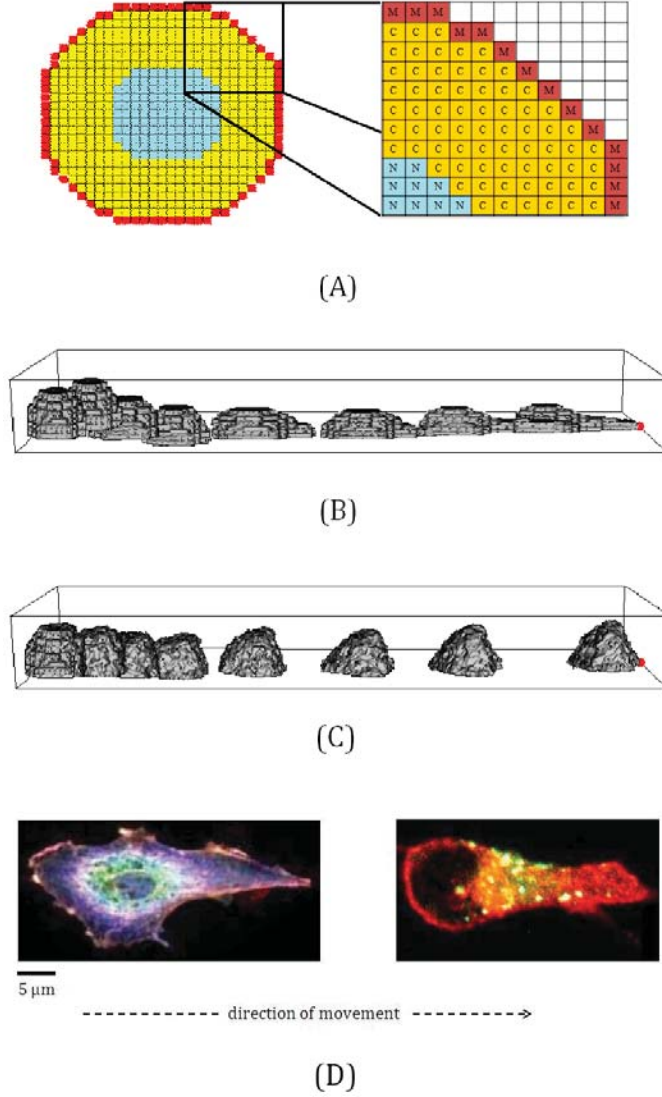
Fig. 7. *Test simulation: chemotactic migration of a compartmentalized EC in a $600 \times 200 \times 80$ lattice site domain Ω (1 lattice site = 0.125 μm^3). (A) xy section of the compartmentalized EC. We can see the different units that form the clustered individual: nucleus ($\sigma = 1$, $\tau(\sigma) = N$), cytosolic region ($\sigma = 2$, $\tau(\sigma) = C$), and PM ($\sigma = 3$, $\tau(\sigma) = M$). (B) EC phenomenology reproduced from representative images taken at 45-min. intervals until $t = 6$ h (1 MCS = 10 s). The cell, after a short latency, rapidly polarizes establishing a leading edge, a long thin pseudopodium, which gives the direction of motion. The red dot represents the VEGF source, placed at $\mathbf{x} = (600, 100, 0)$. The parameter setting used $J_{N,C}^{int} = J_{C,M}^{int} = -20$, $A_{1,1}^{vol} = 900$ μm^3, $A_{1,2}^{vol} = 32000$ μm^3, $A_{1,3}^{vol} = 5653$ μm^3, $A_{1,1}^{sur} = 3140$ μm^2, $A_{1,2}^{sur} = 1110$, $A_{1,3}^{sur} = 2223$ μm^2, μm^3, $\lambda_{1,1}^{vol} = \lambda_{1,2}^{vol} = \lambda_{1,3}^{vol} = \lambda_{1,1}^{sur} = 20$, $\lambda_{1,2}^{sur} = \lambda_{1,3}^{sur} = 1.2$; $\mu_{1,3} = 5$; $T_{1,1} = 0.4$, $T_{1,2} = T_{1,3} = 4$. (C) Model results in the case of basic CPM. The EC is formed by a unique undifferentiated unit. The Hamiltonian is formed only by the geometrical constraint of the unit and by the term relative to the chemotactic force; all other parameters are the same as the previous case. The basic approach is unable to reproduce cell polarization, as the cell is only a deformed mass that moves toward the chemical source. (D) For comparison, experimental images of chemotactic migration of an adult human dermal microvascular EC (HMEC, left) and of a tumor-derived EC obtained from breast lobular-infiltrating carcinoma (B-TEC, right). In both cases, we can see that a pseudopodium-like motility structure has formed in the direction of motion and that the nucleus lags behind, in the trailing zone of the cell. Images courtesy of the Department of Animal and Human Biology, Università degli Studi di Torino.*

energetic counterpart of the chemical force:

$$(3.9) \qquad H(t) = H_{adhesion}^{int}(t) + H_{constraint}(t) + H_{force}^{chemical}(t).$$

In particular, referring to (3.2), we have

$$(3.10) \qquad H_{adhesion}^{int}(t) = \sum_{\substack{\mathbf{x} \in \Omega, \mathbf{x}' \in \Omega'_{\mathbf{x}} \\ \eta(\sigma(\mathbf{x})) = \eta(\sigma(\mathbf{x}')) \\ \sigma(\mathbf{x}) \neq \sigma(\mathbf{x}')}} J_{N,C}^{int} + \sum_{\substack{\mathbf{x} \in \Omega, \mathbf{x}' \in \Omega'_{\mathbf{x}} \\ \eta(\sigma(\mathbf{x})) = \eta(\sigma(\mathbf{x}')) \\ \sigma(\mathbf{x}) \neq \sigma(\mathbf{x}')}} J_{C,M}^{int},$$

where high negative values of $J_{N,C}$ and $J_{C,M}$, the generalized adhesions between the cytosolic region and the nuclear cluster and the PM, respectively, prevent the EC from disconnecting. For the sake of completeness, we should also include the contact energy between the nucleus and the PM; however, we have omitted it (i.e., imposing $J_{N,M}^{int} = 0$), as this is an unrealistic situation, since the nuclear and the plasma membranes do not in fact interact directly during cell motion [2]. We also neglect the external adhesion between the cell PM and the virtual medium (i.e., $J_{C,Q}^{ext} = 0$); as seen, the extracellular environment is in fact assumed to be simply a passive medium-like substrate which does not influence cell behavior. $H_{constraint}$ consists of the geometric constraints of the subcellular units:

$$(3.11) \qquad H_{constraint}(t) = H_{volume}(t) + H_{surface}(t),$$

where

(3.12)

$$H_{vol}(t) = \lambda_{1,1}^{vol} \left[\frac{a_{1,1}^{vol}(t) - A_{1,1}^{vol}}{a_{1,1}^{vol}(t)} \right]^2 + \lambda_{1,2}^{vol} \left[\frac{a_{1,2}^{vol}(t) - A_{1,2}^{vol}}{a_{1,2}^{vol}(t)} \right]^2 + \lambda_{1,3}^{vol} \left[\frac{a_{1,3}^{vol}(t) - A_{1,3}^{vol}}{a_{1,3}^{vol}(t)} \right]^2,$$

(3.13)

$$H_{sur}(t) = \lambda_{1,1}^{sur} \left[\frac{a_{1,1}^{sur}(t) - A_{1,1}^{sur}}{a_{1,1}^{sur}(t)} \right]^2 + \lambda_{1,2}^{sur} \left[\frac{a_{1,2}^{sur}(t) - A_{1,2}^{sur}}{a_{1,2}^{sur}(t)} \right]^2 + \lambda_{1,3}^{sur} \left[\frac{a_{1,3}^{sur}(t) - A_{1,3}^{sur}}{a_{1,3}^{sur}(t)} \right]^2.$$

All the terms in (3.12) and (3.13) resemble (3.6) with $p = 2$. The target dimensions are taken from the typical measures observed in classical cultures for resting ECs in the absence of external forces, as given in [89]. Assuming that the cell does not grow during migration, we keep the cell volume fluctuations negligible by setting high constant values of $\lambda_{1,1}^{vol}$, $\lambda_{1,2}^{vol}$, and $\lambda_{1,3}^{vol}$. Moreover, since the nucleus does not deform to any great extent in response to an external chemical stimulus, $\lambda_{1,1}^{sur}$ is also high. Finally, the ability of ECs to reorganize their shape after VEGF stimulations [28] is taken into account with low values of $\lambda_{1,2}^{sur}$ and $\lambda_{1,3}^{sur}$, which, as seen, represent the inverse elasticities of the cytosolic region and the PM, respectively.

The net energy difference due to the chemical force is the same as in (3.8):

$$(3.14) \qquad \Delta H_{force}^{chemical} = \mu_{1,3}[C(\mathbf{x}_{target}, t) - C(\mathbf{x}_{source}, t)],$$

where $\mathbf{x}_{source}$ and $\mathbf{x}_{target}$ are, respectively, the source and the final lattice sites randomly selected during a trial update in an MCS; $\mathbf{x}_{source}$ belongs to the PM, while $\mathbf{x}_{target}$ is a medium site. $\mu_{1,3}$ represents the chemotactic sensitivity of the cell, which is related to the activity of the surface receptors. C is a measure of the local extracellular concentration of the VEGF, given by c, sensed by the moving cell membrane

site (see [79, 80]):

$$(3.15) \qquad C(\mathbf{x}, t) = \sum_{\mathbf{x}' \in \Omega'_{\mathbf{x}} : \sigma(\mathbf{x}')=0} c(\mathbf{x}', t).$$

The spatial profile of the VEGF concentration satisfies the following diffusion equation:

$$(3.16) \qquad \frac{\partial c(\mathbf{x}, t)}{\partial t} = D_c \nabla^2 c(\mathbf{x}, t) - \lambda_c c(\mathbf{x}, t) + S(\mathbf{x}),$$

where $c(\mathbf{x}, t)$ denotes the actual concentration of the peptide at the medium site $\mathbf{x}$ ($\sigma(\mathbf{x}) = 0$). The coefficients of diffusivity, $D_c = 10 \ \mu\mathrm{m}^2\mathrm{s}^{-1}$, and of degradation, $\lambda_c = 1.8 \cdot 10^{-4} \ \mathrm{s}^{-1}$, are homogeneous throughout the extracellular environment [81]. S describes the production of VEGF at a constant rate $\phi_c = 0.78 \ \mathrm{h}^{-1}$ per unit of time by the punctual source placed in the middle of the bottom-right side of domain Ω (i.e., at site $\mathbf{x} = (600, 100, 0)$); see Figure 6(B). The Boltzmann temperature of the nucleus, $T_{1,1}$, is low, which translates into biologically reasonable small nuclear membrane fluctuations. High values of $T_{1,2}$ and $T_{1,3}$ instead give a quantitative idea of a VEGF-enhanced intrinsic motility of the cell, as they cause a high frequency of random extension and retraction of cytoskeletal pseudopods and of membrane ruffles.

As shown in Figure 7(B), the stimulated endothelial cell undergoes a gradual transition from the initial symmetric stationary state to a polarized migratory state, characterized by clearly distinguishable leading and trailing edges. In particular, a long and thin membrane-bound cytoplasmic pseudopodium emerges at the front of the cell, defining the direction of migration toward the chemotactic source, as the elongated cell moves by constantly protruding at the leading edge, while retracting at the rear. Such a phenomenology, consistent with in vitro realizations performed in [28], where VEGF-stimulated ECs are found to assume an extended bipolar morphology, results from the interplay between the chemotactic-induced membrane extension at the leading front of the cell and the mechanical properties given to its compartments, with a stiff nucleus and more fluid cytoplasmic and membrane regions (i.e., $\lambda_{1,1}^{sur} > \lambda_{1,2}^{sur} = \lambda_{1,3}^{sur}$ while $T_{1,1} < T_{1,2} = T_{1,3}$). From the mechanical view point, the exogenous stimulus causes the right region of the cell plasmamembrane to locally protrude in the direction of increasing VEGF gradients, with a speed of protrusion proportional to the modulus of the local chemical strength, μ_{ch} (for instance, in any CPM model the simulated objects experience an implicit drag force from the lattice, and thus they have Aristotelian dynamics; i.e., their local velocity and not their acceleration is proportional to the local force; refer to (3.22) and to [6, 53] for more details). The leading front of the membrane, through the high generalized adhesion force $J_{C,M}^{int}$, then drives the motion of the cytosolic region. The cell cytosol, due to its high motility and elasticity, in turn deforms and moves forward, while pulling on the nucleus with the same force (exerted through the contact tension $J_{N,C}^{int}$). However, the nuclear cluster (which, as a CPM object, also follows Aristotelian dynamics) is basically stuck to the underlying lattice as a consequence of its rigidity and low motility; therefore, it lags behind, creating the characteristic polarized morphology of the EC. The chemotactic-induced extension of the leading front of the cell then causes an average displacement of the lateral and trailing regions toward the chemical source (due to the volume constraint of the membrane and the cytosolic clusters). In particular, when the rear part of the individual has moved far enough to the right, the nucleus, in order to preserve its energetically favorable contact with the lagging

part of the cytosol, that has remained interposed between the nucleus itself and the PM (since both $J_{N,C}^{int}$ and $J_{C,M}^{int} \ll 0$), is forced to move in the same direction. We have therefore a conversion from nuclear sites to cytoplasmic sites which propagates from the left to the right to preserve the nuclear volume. These mechanisms are a simplified picture of the biological processes underlying cell movement (the relative literature is vast; however we refer the reader to the comprehensive biochemical reviews [68, 72] and the classical books [2, 40]), which can be differentiated into two stages. In the first, the external chemical stimulus, via surface receptors, triggers the active polymerization of the cell cytoskeleton, which results in the constant abutting of the cell PM in the direction of motion and in the coordinated development and release of focal adhesions (FAs). In particular, during this first phase, the nucleus is unable to have a directional movement, as it fluctuates only negligibly in the cytoplasmic fluid. In the second phase, the cytoskeletal components drag the trailing regions of the cell and pull the nucleus via mechanical forces transmitted by the intermediate actin filaments and microtubules to which it is anchored, as clearly reproduced in the representative experimental images in Figure 7(D) and reviewed in [93] and the references therein. Indeed, the absence of significant nucleus displacements in the first stage of cell motion is reproduced in the model by the artifact of staking the nuclear cluster to the underlying lattice with a high rigidity, while its subsequent passive motion is instead achieved by giving a high contact energy $J_{N,C}^{int}$, which forces the nucleus to simultaneously move with the lagging cytosolic region. Obviously, a more realistic model should explicitly include the dynamics of the cell cytoskeleton and its signal transduction (this topic, often approached in the literature with multiphase models (see, for example, the book [16]), could represent a fundamental improvement of CPM applications, since it has received little though increasing attention). In the presented example, the importance of the compartmentalized approach is underlined by studying the phenomenology of the cell in the case of a monocompartmental representation (i.e., the EC is formed by a single, undifferentiated cytoplasm, while all the other model assumptions are not changed): as reproduced in Figure 7(C), the polarization process does not emerge and the cell is a deformed mass which moves in the direction of the chemical source (notice that also the top of the cell unrealistically protrudes). As a further confirmation of the advantages of applying the compartmentalized model, some authors using the basic CPM have needed to introduce an ad hoc rule on cell length to make cells polarize [57].

In order to explain the use of the external adhesion energy, we now turn to apply the above-presented model of cell chemotactic migration in the case of a two-component inhomogeneous extracellular environment, which is constituted by a network of collagen-like fibers and by the classical isotropic medium. The endothelial cell is therefore planted in the left side of a $300 \times 200 \times 80$ site domain Ω, where 100 matrix threads have been randomly arranged. As in the previous application 1 lattice site $= 0.125 \ \mu m^3$ and 1 MCS $= 10$ s. The collagenous cords are standard, noncompartmentalized CPM objects $\sigma = 4, \ldots, 103$, of type $\tau(\sigma) = F$. They are 80 lattice sites long and 4 lattice sites wide and fixed (i.e., $T_{\sigma=4,\ldots,103} = 0$). The Hamiltonian is the same as in (3.9), except for the addition of the appropriate term relative to the adhesive interactions between the cell PM and the collagenous fibers:

$$(3.17) \qquad H_{adhesion}^{ext}(t) = \sum_{\substack{\mathbf{x} \in \Omega, \mathbf{x}' \in \Omega'_{\mathbf{x}} \\ \eta(\sigma(\mathbf{x})) \neq \eta(\sigma(\mathbf{x}')) \\ \sigma(\mathbf{x}) \neq \sigma(\mathbf{x}')}} J_{M,F}^{ext}.$$

Moreover, since cell motion through small fiber pores requires not only a strong deformation of the cytosol and of the PM but also the ability of the nucleus to squeeze, we also set a low value of $\lambda_{1,1}^{sur}$. All the other model parameters are the same as in the previous model application, as is the evolution of the VEGF, whose source is placed at $\mathbf{x} = (300, 100, 0)$. The phenomenological result is given in Figure 8, where we also prove the comparison with an experimental image.
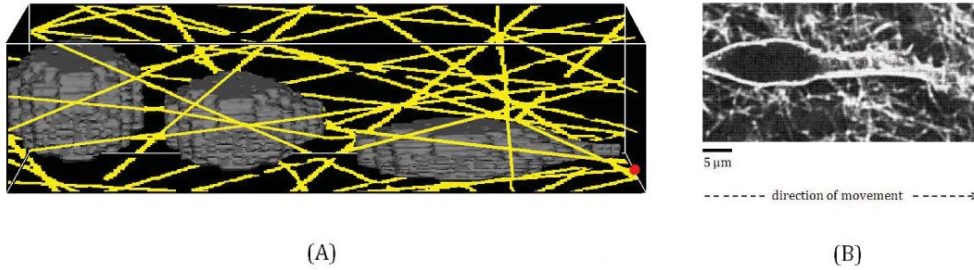

(A)   (B)

FIG. 8. *Test simulation:* (A) *Computational results and of the chemotactic migration of the compartmentalized endothelial cell in a* $300 \times 200 \times 80$ *site domain* Ω, *representing a two-component extracellular environment.* 100 *matrix threads have been randomly arranged throughout the simulated isotropic. As in the previous application,* 1 *lattice site* $= 0.125$ μm^3 *and* 1 $MCS = 10$ *s. Representative three-dimensional views taken at* 30 *min intervals until* $t = 1.5$ *h. The red dot represents the chemical source. The parameter setting used is the same as in Figure* 6, *except for* $J_{M,F}^{ext} = 5$ *and* $\lambda_{1,1}^{sur} = 1$. (B) *Representative experimental image of the migration of a human umbilical vein's Endothelial Cells (HUVEC) planted in three-dimensional fibrous matrix. Figure kindly provided by the Department of Animal and Human Biology, Università degli Studi di Torino.*

3.2. Adding subcellular mechanisms. In order to improve the realism of CPM applications, research has mainly focused on defining more complex Hamiltonians able to reproduce increasingly specific rules for object behavior and interactions [52]. However, as pointed out in [33, 59], little has been done to obtain an accurate description of the internal state of individuals, whose evolution directly controls their phenomenology. In fact, microscopic mechanisms have only been modeled to influence the behavior of CPM objects via appropriate extra terms in the Hamiltonian [53], or with changes in cell mitotic rates [41] or types. In this regard, an intriguing approach has been used in a model for chick limb-bud development [14, 15]: a threshold local concentration of activator TGF-β in fact drove the differentiation of responsive cells in the active zone, eventually varying their properties (i.e., they became fibronectin-producing and upregulated the intercellular adhesion). In interesting models of thrombus formation [96, 97, 98], the activation of platelets was instead controlled by the level of chemical components, which derived from biochemical reactions of coagulation pathways in blood flow and on cell surface. Such approaches have given qualitatively correct results and represent a useful starting point for further improvements of the method. However, we here assume that the internal state of a biological individual (i.e., the microscopic level) regulates its biophysical properties (described by mesoscopic Potts coefficients) and not directly its dynamics (described by the terms in the Hamiltonian). An analogous idea was introduced in [39] for a specific case but was barely developed. On the basis of this hypothesis, we propose a comprehensive and general procedure to incorporate microscopic models for individual internal states within the mesoscopic CPM.

Let σ denote a certain discrete object (which, as seen, can now represent a whole

individual or one compartment): we define its internal state vector $\mathbf{s}_\sigma \in \mathbb{R}^n$. The length n of $\mathbf{s}_\sigma$ is defined by the number of internal factors (i.e., nutrients, proteins, and growth factors) considered in the microscopic model and represents a sort of internal degree of freedom of σ. Each component $s_{\sigma,l}$, where $l = 1, \ldots, n$, can be local (i.e., per site) and/or time-dependent (i.e., specified as a known function and thus linked to a specific regulatory pathway, which needs to be modeled, as will be explained later). Hence, in general, $\mathbf{s}_\sigma = \mathbf{s}_\sigma(\mathbf{x}, t)$, where $\mathbf{x} \in \sigma$. The spatial localization of $\mathbf{s}_\sigma$ is mandatory to accurately represent internal inhomogeneities of σ, while its time-dependence reproduces its microscopic evolution.

For any σ, let us consider a generic Potts coefficient $\alpha \in \{\lambda_\sigma^i; T_\sigma; \mu_\sigma^k\}$. We now define $\mathbf{s}_\sigma^\alpha \in \mathbb{R}^m$, where $m \leq n$, the subvector of $\mathbf{s}_\sigma$ whose components influence the biophysical property of σ described by α. Therefore, α can be expressed as

$$(3.18) \qquad \alpha(\mathbf{s}_\sigma^\alpha) = f_\alpha(\mathbf{s}_\sigma^\alpha),$$

where $f_\alpha : \mathbb{R}^m \mapsto \mathbb{R}$ is a continuous function, which obviously needs to be appropriately defined in relation to the case of interest (an example is given in section 4). In particular, if f_α is an increasing (respectively, decreasing) function of the component $s_{\sigma,j}^\alpha$, where $j = 1, \ldots, m$, we can therefore say that $s_{\sigma,j}^\alpha$ enhances (respectively, inhibits) α. In some cases it is useful to order the components of $\mathbf{s}_\sigma^\alpha$ and to write it as $\mathbf{s}_\sigma^\alpha = (\mathbf{s}_\sigma^{\alpha,A}, \mathbf{s}_\sigma^{\alpha,I})$, where $\mathbf{s}_\sigma^{\alpha,A} \in \mathbb{R}^k$ (respectively, $\mathbf{s}_\sigma^{\alpha,I} \in \mathbb{R}^{m-k}$, with $k \leq m$) consists in the activators (respectively, the inhibitors) of the biophysical property defined by α.

According the same notation we have that, if $\gamma \in \{J_{\tau(\sigma),\tau(\sigma')}^{int}, J_{\tau(\sigma),\tau(\sigma')}^{ext}\}$, then

$$(3.19) \qquad \gamma(\mathbf{s}_\sigma^\gamma, \mathbf{s}_{\sigma'}^\gamma) = g_\gamma(\mathbf{s}_\sigma^\gamma, \mathbf{s}_{\sigma'}^\gamma),$$

where $g_\gamma : \mathbb{R}^m \times \mathbb{R}^m \mapsto \mathbb{R}$ and σ and σ' are two objects in contact. In particular, the adhesive strengths are determined by the internal state of both elements, as they are not only a property of each single individual. Moreover, differentiating the components of the internal state vector that either enhance or downregulate the relative contact forces, we have that, if $g_\gamma = g_\gamma(\mathbf{s}_\sigma^{\gamma,A}, \mathbf{s}_{\sigma'}^{\gamma,A})$, then g_γ is a decreasing function of its components, while, if vice versa $g_\gamma = g_\gamma(\mathbf{s}_\sigma^{\gamma,I}, \mathbf{s}_{\sigma'}^{\gamma,I})$, then it is an increasing function.

Equations (3.18) and (3.19) state that the variation of the Potts coefficients of the element σ (as usual, either an entire individual or one of its compartments) is due to the evolution of its internal state; in this way the mesoscopic biophysical properties of σ are no longer given a priori (or varied with prescribed rules) but are autonomously and continuously inherited from the flow of information coming from the microscopic molecular level. They therefore assume a biologically more realistic and accurate characterization and, in principle, can be more easily compared with experimentally measurable quantities. Procedurally, at every simulation time step t, the microscopic model of each object σ is run. The outcome is then used to modulate the values of the relative Potts coefficients which, in turn, rescale the pattern energy H. After the subsequent spin flip, the microscopic model is rederived, based on the new position of the object. The different levels of organization thus continuously give feedback and influence each other.

The application of the new approach to biological cells, depicted in Figure 9, is of particular interest. In this context, each component of the internal state vector $\mathbf{s}$ can represent the spatio-temporal variation of the concentration of intracellular ions and molecules (nutrients, nucleic acids, proteins, growth factors, etc.), whose presence and quantity strictly regulate the cell activity and its biological properties. In particular, for any component $s_{\sigma,l}$ of $\mathbf{s}_\sigma$, given a well-characterized (although simplified)
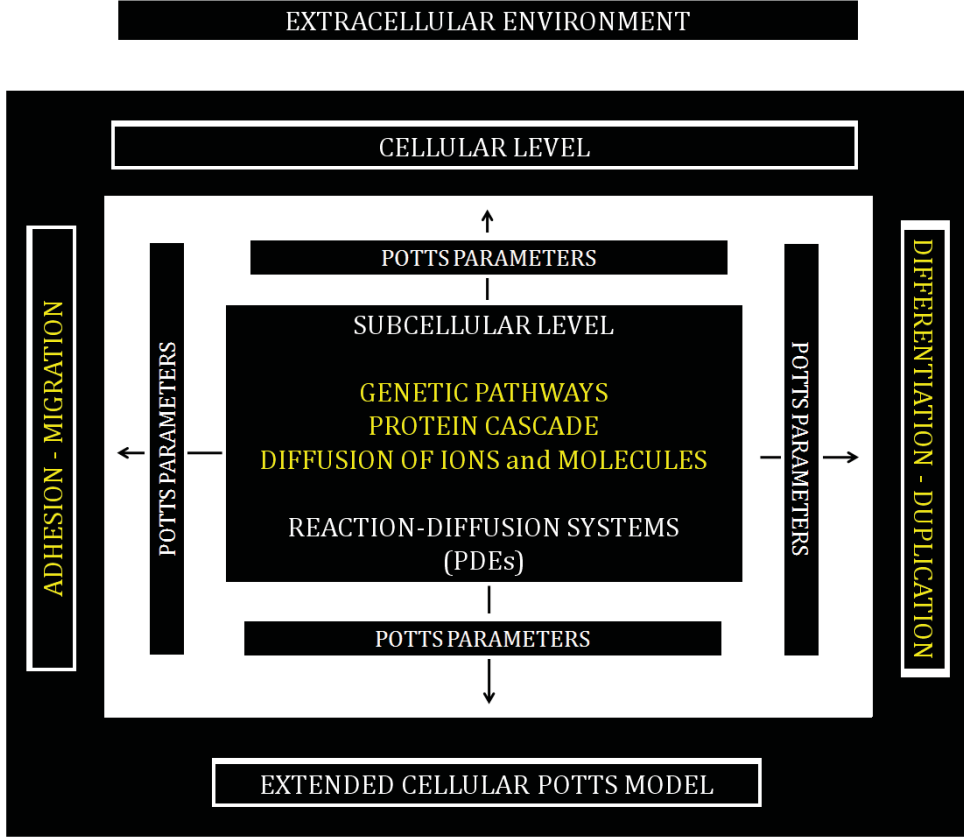
FIG. 9. *Hierarchy of scales and environments, the corresponding biological mechanisms, and our proposed modeling approach. Information flows from the microscopic biochemical processes to the cell-level phenomenology.*

biochemical pathway

$$(3.20) \qquad A + B \rightleftharpoons C + D \cdots \leftrightharpoons E + F \rightleftharpoons s_{\sigma,l},$$

it is always possible to set a suitable model, whose outcome is $s_{\sigma,l}$ itself. For the sake of simplicity, it is not restrictive to combine groups of reactions in (3.20), whose results have the same effect on the final result of the network. Biochemical kinetics can be accurately described by reaction-diffusion (RD) systems, which usually specialize in several coupled differential equations. As an example of the potentials of the proposed model development, the Boltzmann temperature T in (2.1) is no longer a biologically meaningless agitation rate but a variable property of each moving cell and therefore assumes a well-defined value of *cell intrinsic motility*, which is mediated by a wide range of intracellular substances (i.e., calcium ions, fatty acids, etc.).

Microscopic models of intracellular dynamics can be used together with the compartmentalized approach described in the previous section (if σ represents a subregion of compartmentalized individual η, the internal state vector is $\mathbf{s}_{\eta,\sigma}$) to further improve the models by adding more realistic details. In fact, if σ represents a cell subunit, the biochemical processes defined in (3.20) are accurately localized within a well-defined subcellular compartment, as occurs in reality. Such an integration between

the two proposed extensions of the CPM therefore allows us to handle several biological mechanisms, which are difficult to reproduce with the basic CPM. For example, the explicit representation of the cell PM permits us to straightforwardly model a wide range of surface receptor-activated intracellular pathways, as well as specific protein cascades that mediate the activity of the cell adhesion molecules. Moreover, the geometrical properties of the cell cytosolic compartment, such as its elasticity, can now evolve according to a model of the active reorganization of the actin filaments, which is powered, for example, by ATP (adenosine triphosphate) hydrolysis. A more realistic representation of the mitotic process is also possible. In most existing CPMs, the cell cycle is not modeled explicitly, since cells usually undergo duplication when they reach a fixed volume [7, 75, 82]. With the presented CPM improvements, it is instead possible to incorporate appropriate intracellular signaling cascades regulating cell cycle-dependent events.

The proposed method to interface the basic mesoscopic CPM with models of microscopic dynamics can be considered a general guide to reproduce complex interactions between the different levels of organization that are typical of biological phenomena. It can in fact be applied to a number of situations, given the knowledge of

- the pathways of interest and
- the specific functional laws that describe their influence on the biophysical properties of individuals, i.e., the functions f and g.

In section 4 we will give a sample application of the above-defined procedure that will also be useful in clarifying the complex notation adopted in this section.

3.3. Motility of individuals. The motility of individuals plays an important role in all biological phenomena. For example, the migratory properties of cells are involved, to various extents, in both physiological (such as embryo development and organogenesis, organism growth and survival, or wound healing) and pathological (such as inflammation and atherosclerosis, cancer invasion, or metastatization) fundamental processes. An accurate description of the motility of individuals is therefore a fundamental issue for all computational approaches, and it is one of the most attractive features of the CPM. The Metropolis algorithm is in fact able to naturally represent the continuous, exploratory behavior of migrating organisms through biased extensions and retractions of their boundaries. Moreover, by updating only one spin at a time, the individuals move gradually, rather than in jumps, as in some other approaches (for instance, multispin dynamics like Kawasaky dynamics are also possible, as mentioned in [33]). The CPM technique also allows us to differentiate between the isotropic intrinsic motility of each individual, which is described by its Boltzmann temperature T (which can be approximately compared to a diffusion coefficient with a continuous point of view), and the directional, force-based component of its motion. Since a difference in a potential energy might be related to a force; at any given time t, for any site $\mathbf{x}$ of the domain Ω, the local negative gradient of the functional H can be related to the local applied force

$$(3.21) \qquad \mathbf{F}_{\mathbf{x}\in\Omega}(t) = -\overrightarrow{\nabla} H_{\mathbf{x}\in\Omega}(t),$$

where $H_{\mathbf{x}\in\Omega}$ is the Hamiltonian restricted to site $\mathbf{x}$ (i.e., formed only by the terms involving $\mathbf{x}$). In particular, for any element σ (as usual, both a whole individual or a subcompartment), the local velocity, and not the acceleration, is proportional to the local force, resulting in the so-called Aristotelian dynamics. This relation is also known as *overdamped force-velocity response*, and it is characteristic of other IBMs

[25, 26]:

$$(3.22) \qquad \frac{d\mathbf{r}_{\mathbf{x}\in\sigma}}{dt} = \mathbf{v}_{\mathbf{x}\in\sigma}(t) = k_{\mathbf{x}\in\sigma}\mathbf{F}_{\mathbf{x}\in\sigma}(t) = -k_{\mathbf{x}\in\sigma}(t)\overrightarrow{\nabla}H_{\mathbf{x}\in\sigma}(t).$$

The coefficient $k_{\mathbf{x}\in\sigma}(t)$ is the *net rate of transition* of site $\mathbf{x}$ (i.e., the difference between its probability of moving and that of staying still, $P(\sigma(\mathbf{x}) \to \sigma(\mathbf{x}')) - P(\sigma(\mathbf{x}) \nrightarrow \sigma(\mathbf{x}'))$, as in [33]). As analytically demonstrated again in [33] (and in [53] for a particular case), $k_{\mathbf{x}\in\sigma}(t)$ is related to the Boltzmann temperature. We can therefore write

$$(3.23) \qquad \mathbf{v}_{\mathbf{x}\in\sigma}(t) \propto -T_\sigma(t)\overrightarrow{\nabla}H_{\mathbf{x}\in\sigma}(t).$$

As far as the above-mentioned published results are concerned, we here prefer to use a proportional dependence between $k_{\mathbf{x}\in\sigma}(t)$ and $T_\sigma(t)$ and not an equation, since the exact relation between the Monte Carlo spin copy attempts and continuous time, as well as the kinetics application of the Metropolis-like algorithm, are still debated and persistent sources of criticism. Some comments on the consequences of relation (3.23) are given here:

- It is characteristic of an extremely viscous regime, such as the biological environment, where the individuals thus evolve under strong damping.
- It is definitive confirmation that discrete CPM objects move in order to minimize the total energy. The modulus of the local velocity of σ, at any given time t, depends on the magnitude of the sensed local energy gradient, as well as on its intrinsic motility $T_\sigma(t)$, which, in our extended approach, is coherently a variable property of each unit σ.
- Given that the energy functional H is the sum of the terms that represent multiple biological mechanisms with the same architecture, it is straightforward to evaluate the contribution of each of them to the local velocity of unit σ. In fact, for any mechanism i, by equating all the other terms to zero, we obtain

$$(3.24) \qquad \mathbf{v}_{\mathbf{x}\in\sigma}\big|_{i-mechanism}(t) \propto -T_\sigma(t)\overrightarrow{\nabla}H^{i-mechanism}_{\mathbf{x}\in\sigma}(t).$$

  In particular, it is possible to differentiate the contributions of either short-range or long-range mechanisms,

$$(3.25) \qquad \mathbf{v}_{\mathbf{x}\in\sigma}(t) \propto -T_\sigma(t)\left[\overrightarrow{\nabla}H^{short\ range}_{\mathbf{x}\in\sigma}(t) + \overrightarrow{\nabla}H^{long\ range}_{\mathbf{x}\in\sigma}(t)\right],$$

  the former of which includes, for example, adhesion and haptotaxis, while the latter includes chemotaxis.

However, even with the new meaning and expression assumed by the Boltzmann temperature, the model in (2.1) can be further improved with the use of alternative laws that are better able to describe experimental observations on the ruffling of individual membranes. In particular, the main weakness of (2.1) is that, in the case of nonpositive net energy differences caused by the proposed displacement ($\Delta H|_{\sigma(\mathbf{x})\to\sigma(\mathbf{x}')} \leq 0$), each element σ is certainly going to move, regardless of its T_σ. This lacks biological realism, since the effective motion of an organism is closely dependent on its motility. For example, a "frozen" cell (i.e., with negligible intrinsic motility) does not extend its pseudopods toward a chemical source if it senses a high chemotactic gradient (which, in the absence of other external forces, results in $\Delta H \ll 0$). This situation is the model counterpart of experimental cells pretreated with cytochalasin B, or held

at 4 °C, as clearly shown in [62]. This issue can easily be addressed using a modified family of transition probabilities $P(\sigma(\mathbf{x}) \to \sigma(\mathbf{x}'))$, which takes into account the object motility T_σ also in the case of energetically favorable displacement attempts. The proposed modeling option is

(3.26)

$$P(\sigma(\mathbf{x}) \to \sigma(\mathbf{x}'))(t) = \begin{cases} p(T_\sigma(t))e^{-\Delta H|_{\sigma(\mathbf{x}) \to \sigma(\mathbf{x}')}/T_\sigma(t)}, & \Delta H|_{\sigma(\mathbf{x}) \to \sigma(\mathbf{x}')} > 0, \\ \\ p(T_\sigma(t)), & \Delta H|_{\sigma(\mathbf{x}) \to \sigma(\mathbf{x}')} \leq 0, \end{cases}$$

where $p(T_\sigma(t)) : \mathbb{R}^+ \mapsto [0,1]$, a sort of *maximum transition probability*, is a continuous and increasing function of T_σ and is characterized by

(3.27)
$$\begin{cases} p(0) = 0, \\ \\ \lim_{T_\sigma \to +\infty} p(T_\sigma) = 1. \end{cases}$$

With reference to the above-mentioned example, (3.26) and (3.27) state that if $T_\sigma \to 0$, cell σ does not move, even if it senses a steep energy gradient, as it is really frozen. According again to the discussion in [33, 53], we obtain

(3.28) $$\frac{d\mathbf{r}_{\mathbf{x} \in \sigma}}{dt} = \mathbf{v}_{\mathbf{x} \in \sigma}(t) = k'_{\mathbf{x} \in \sigma}(t)\mathbf{F}_{\mathbf{x} \in \sigma}(t) = -k'_{\mathbf{x} \in \sigma}(t)\overrightarrow{\nabla} H_{\mathbf{x} \in \sigma}(t),$$

where $k'_{\mathbf{x} \in \sigma}(t)$ is the new *net rate of transition* coming from the proposed probability function in (3.26). Furthermore, considering the expression of (2.1) itself and comparing it with (3.26) (i.e., the latter is equal to the former multiplied by factor $p(T_\sigma(t))$), it is straightforward to notice that $k'_{\mathbf{x} \in \sigma}(t) = p(T_\sigma(t))k_{\mathbf{x} \in \sigma}(t)$ and that therefore $k'_{\mathbf{x} \in \sigma}(t) \propto p(T_\sigma(t))T_\sigma(t)$. Summing up, we finally obtain

(3.29) $$\mathbf{v}_{\mathbf{x} \in \sigma}(t) \propto -p(T_\sigma(t))T_\sigma(t)\overrightarrow{\nabla} H_{\mathbf{x} \in \sigma}(t),$$

where the local velocity of σ is again dependent on its motility $T_\sigma(t)$, which is now scaled by the value of $p(T_\sigma(t))$. In Figure 10 we plot an example of the Boltzmann-like probability given in (3.26) as a function of both temperature T_σ and the magnitude of the energy difference. In particular, we choose $p(T_\sigma(t)) = \tanh(T_\sigma(t))$.

However, it is useful to underline that alternative functions of p can also be used by authors: obviously, each of them will have various degrees of success, when compared to experimental data.

4. An example: Wound healing assay. In order to show how the general theory illustrated in the previous sections can be applied, we here present a comprehensive test model. We simulate a *wound healing assay* of a culture of a poorly differentiated thyroid carcinoma-derived cell line, called ARO [23, 44], stimulated by saturating levels of HGF/SF (hepatocyte growth factor/scatter factor [20, 55]). A wound healing experiment is considered a simple and reliable test for a quantitative evaluation of cell motility, in particular in response to molecules putatively involved in migratory processes. Procedurally, a cell population, coated with a matrix, grows to confluence in a culture plate. The monolayer is then wounded with a sharp object (for example, a pipette tip) and stimulated with nanomolar concentrations of the molecule of interest. The recolonization of the lesion by the remaining cell mass is
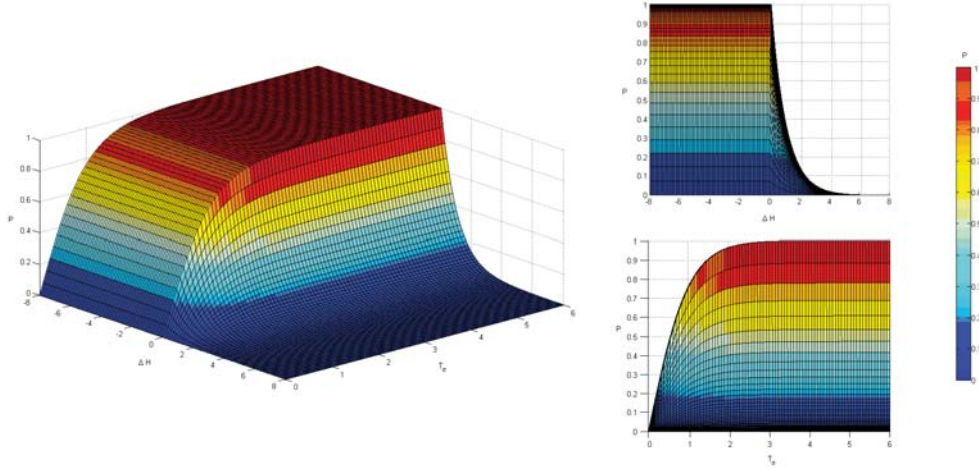
Fig. 10. *Diagram showing the variation of the Boltzmann-like transition probability equation (3.27) as a function of both the intrinsic motility of the individual, T_σ, and the sensed net energy gradient due of the displacement attempt, $\Delta H|_{\sigma(\mathbf{x}) \to \sigma(\mathbf{x}')}$. In particular, we choose $p(T_\sigma(t)) = \tanh(T_\sigma(t))$. The small panels represent the Boltzmann-like curves in the case of fixed $T_\sigma = 4$ (top) and fixed $\Delta H = -2$ (bottom).*

then monitored by means of time-lapse microscopy: images are captured at regular intervals during cell migration and then used for an accurate analysis of the population migratory capacity, which is measured as the rate of advance of the wound edge or by the quantification of the recolonized area.

The HGF/SF is a potent growth factor that elicits multiple cellular responses, including scattering, motility, and morphogenesis [10, 21, 88, 90]. Such a combination of events, also known as *invasive growth*, is fundamental during the embryonic development of most epithelial tissues. When inappropriately activated, this genetic program confers an invasive ability to normal and neoplastic epithelial cells [23, 86, 94]. The high affinity receptor for HGF/SF is the tyrosine kinase Met [24, 46]. Met activation causes the disruption of intercellular adhesion complexes (cadherin-cadherin interactions), and it initiates a number of intracellular signaling pathways. Among others, Phosphatidylinositol 3-kinases (PI3K) and MAPK cascades have been studied intensively and well characterized [20, 99]. Without going into detail, the activity of the multidocking sites of the Met triggers the biosynthesis, in the cell sub-plasmamembrane regions, of PI3K (via the production of Gab1) and of MAPK (via the activity of the adaptor proteins Grb2 and Ras). PI3K and MAPK molecules then diffuse within the cell cytosol, where they induce the production of Cdc42 and Rac small GTP-ases [23, 99], which in turn stimulate the migratory capacity of the cells. In particular, Cdc42, which can lead to the activation of Rac itself [5], is considered to be a central regulator of cell protrusive activity [29, 74]. Rac is instead required for lamellipodia and membrane ruffles [9]. Both Cdc42 and Rac mediate actin polymerization by activating the actin-related protein, Arp2/3 complex [38, 73, 74]. Figure 11 diagrammatically represents the previously described key biochemical processes.

The multilevel modeling environment takes into account all the proposed developments of the CPM: at the mesoscopic, cellular level, a compartmentalized CPM represents the phenomenology of the population of AROs, focusing on their shape, membrane fluctuation, and adhesive interactions. Moreover, the internal state of
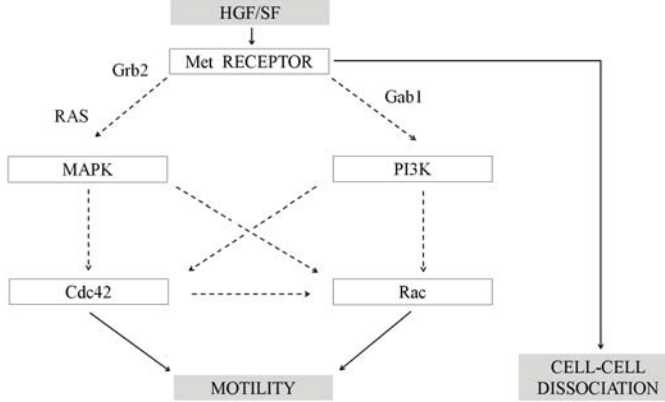
Fig. 11. *Simplified schematic representation of HGF/SF signaling cascades in the control of ARO cell motogenesis. Met receptors activate a series of intracellular events that induce the recruitment of Phosphatidylinositol 3-kinase (PI3K) and Mitogen-activated protein kinase (MAPK). Both intracellular messengers are able to activate Rac and Cdc42 molecules. Increases in Rac and Cdc42 activity trigger cell motility. The dashed arrows stand for indirect pathways are not completely included in the model.*

each cell is explicitly approached with a continuous model, which reproduces the biochemical signaling pathways activated, via Met receptors, by the HGF/SF, whose extracellular evolution is in turn described by a standard continuous equation. All the levels are then inextricably linked so that the behavior of the AROs is realistically driven by their microscopic, molecular dynamics.

4.1. Cell-level model. The core of our simulation framework is obviously the extended CPM, which naturally handles cellular and multicellular behavior and interactions. Since we wish to compare our simulations with experimental wound healing assays, we use a bidimensional domain $\Omega \subseteq \mathbb{R}^2$. The AROs are compartmentalized individuals η of type $\theta(\eta) = E$. In particular, each cell is subdivided into the three well-defined units σ defined in section 3.1.1: the nucleus, a central round cluster of type $\tau(\sigma) = N$, the surrounding, initially circular, cytosolic region of type $\tau(\sigma) = C$, and the PM of type $\tau(\sigma) = M$. Again in this case, the nuclear membrane is not explicitly modeled, as it is simply defined as the interface between the cytosolic compartment and the nuclear region. In fact, with respect to the PM, no relevant phenomena occur there, while it is important to look more carefully at the processes occurring at the PM. For any cell η, we define the state vector of each compartment:
- if σ is such that $\tau(\sigma) = M$, $\mathbf{s}_{\eta,\sigma}(\mathbf{x},t) = (m(\mathbf{x},t)) \in \mathbb{R}$, where $m(\mathbf{x},t)$ is the local concentration of the activated surface receptors Met;
- if σ is such that $\tau(\sigma) = \{C, N\}$, $\mathbf{s}_{\eta,\sigma}(\mathbf{x},t) = (p(\mathbf{x},t), k(\mathbf{x},t), c(\mathbf{x},t), r(\mathbf{x},t)) \in \mathbb{R}^4$, where $p(\mathbf{x},t)$ corresponds to the local concentration of PI3K, $k(\mathbf{x},t)$ of MAPK, $c(\mathbf{x},t)$ of Cdc42, and $r(\mathbf{x},t)$ of Rac.

All these quantities are expressed in units of μM. The extracellular environment, i.e., the experimental-like Matrigel, is modeled as a special generalized cell $\sigma = 0$ of type $\tau = Q$. As usual, it is assumed to be static, passive, and homogeneously distributed throughout the simulation domain and therefore without volume or surface attributes. Also in this case, we neglect cell-matrix interactions or matrix remodeling mechanisms such as the secretion of protein or degrading enzymes.

TABLE 4.1
Parameters involved in the model of section 4.

Parameter	Description	Model value	Reference
$A_{\eta,N}^{vol}$	volume of nuclear compartment	50 [μm^2]	fit to [23, 78]
$A_{\eta,N}^{sur}$	surface of nuclear compartment	43 [μm]	fit to [23, 78]
$A_{\eta,C}^{vol}$	volume of cytosolic compartment	150 [μm^2]	fit to [23, 78]
$A_{\eta,C}^{sur}$	surface of cytosolic compartment	90 [μm]	fit to [23, 78]
$A_{\eta,M}^{vol}$	volume of plasmamembrane	60 [μm^2]	fit to [23, 78]
$A_{\eta,M}^{sur}$	surface of plasmamembrane	60 [μm]	fit to [23, 78]
$\lambda_{\eta,\sigma}^{vol}$	volume elasticity	20	
$\lambda_{\eta,\sigma}^{sur}$	surface elasticity	20	
$J_{C,N}^{int} = J_{C,M}^{int}$	generalized intracellular adhesion	-20	
J_0	basal adhesive strength	4.5	fit to [23, 78]
k	coefficient for $J_{M,M}^{ext}$	1/2	
T_0	basal ARO motility	0.4	fit to [23]
h	Michaelis–Menten coefficient for T	1/2	
$T_{\eta,N}$	generalized motility of the nucleus	0.25	
D_H	diffusion constant of HGF	10^{-13} [m^{2}s^{-1}]	[78]
λ_H	on-rate constant of HGF degradation	10^{-4} [s^{-1}]	[78]
ϕ_H	on-rate constant of HGF addition	10^{-4} [s^{-1}]	[78]
z	coefficient of the amount of bound HGF	1 [s^{-1}]	
nr	total number of Met receptors	311.200	
D_p	diffusion constant of PI3K	5 [μm^{2}s^{-1}]	[48]
λ_p	on-rate constant of PI3K degradation	1 [s^{-1}]	[48]
μ_p	maximal rate of PI3K activation	10 [μMs^{-1}]	fit to [12]
$\mu_{p,0}$	Mich.–Ment. const. for PI3K activation	2 [μM]	fit to [12]
D_k	diffusion constant of MAPK	2 [μm^{2}s^{-1}]	[42, 54]
λ_k	on-rate constant of MAPK degradation	1 [s^{-1}]	[42, 54]
μ_k	maximal rate of MAPK activation	10 [μMs^{-1}]	fit to [12]
$\mu_{k,0}$	Mich.–Ment. const. for MAPK activation	2 [μM]	fit to [12]
D_r	diffusion constant of Rac	10^5 [nm^{2}s^{-1}]	[53]
λ_r	on-rate constant of Rac degradation	1 [s^{-1}]	[53]
μ_{p-r}	rate of PI3K-dependent Rac activation	4.5 [s^{-1}]	
μ_{k-r}	rate of MAPK-dependent Rac activation	4.5 [s^{-1}]	
μ_{c-r}	rate of Cdc42-dependent Rac activation	4.5 [s^{-1}]	[53]
D_c	diffusion constant of Cdc42	10^5 [nm^{2}s^{-1}]	[53]
λ_c	on-rate constant of Cdc42 degradation	1 [s^{-1}]	[53]
μ_{p-c}	rate of PI3K-dependent Cdc42 activation	2.5 [s^{-1}]	
μ_{k-c}	rate of MAPK-dependent Cdc42 activation	3 [s^{-1}]	

The system Hamiltonian is given by

(4.1) $$H(t) = H_{constraint}(t) + H_{adhesion}(t).$$

$H_{constraint}$ includes the constraints that regulate cell volume and surface (which, in two dimensions, correspond to the cell area and perimeter). They have the same form as (3.12) and (3.13). The cell target dimensions, given in Table 4.1, reflect the most common morphologies observed in classical cultures of ARO cells [23] and have been kindly measured by the same group of biologists for a previous paper of ours [78]. Cells are not seen to grow during an experimental wound healing assay [23], and HGF/SF stimulation does not cause a dramatic cytoskeletal reorganization; thus, for any cell η and for any unit σ, it is not restrictive to assume high constant values of $\lambda_{\eta,\sigma}^{vol}$ and $\lambda_{\eta,\sigma}^{sur}$ (cf. Table 4.1).

$H_{adhesion}$ is straightforwardly differentiated into the internal and external contact energy contributions; cf. (3.1), (3.2), and (3.3). In particular, $J_{\sigma(\mathbf{x}),\sigma(\mathbf{x}')}^{ext}$, where $\tau(\sigma(\mathbf{x})) = \tau(\sigma(\mathbf{x}')) = M$, is related to the capability of cells $\eta(\sigma(\mathbf{x}))$ and $\eta(\sigma(\mathbf{x}'))$ of

creating local intercellular cadherin-cadherin complexes, that is downregulated by the activation of Met receptors. Hence, adopting the same notation used in section 3.2, for any ARO η and for $\tau(\sigma) = M$, we obtain that

- $\mathbf{s}_{\eta,\sigma}^{J^{ext},I}(\mathbf{x},t) = \mathbf{s}_{\eta,\sigma}^{J^{ext}}(\mathbf{x},t) = \mathbf{s}_{\eta,\sigma}(\mathbf{x},t) = (m(\mathbf{x},t));$

- $J^{ext}(\mathbf{s}_{\eta,\sigma}^{J^{ext},I}(\mathbf{x},t), \mathbf{s}_{\eta',\sigma'}^{J^{ext},I}(\mathbf{x},t)) = g_{J^{ext}}(\mathbf{s}_{\eta,\sigma}^{J^{ext},I}(\mathbf{x},t), \mathbf{s}_{\eta,\sigma'}^{J^{ext},I}(\mathbf{x},t)) = g_{J^{ext}}(m(\mathbf{x},t),$ $m(\mathbf{x}',t)) = J_0 \exp(km(\mathbf{x},t)m(\mathbf{x}',t))$, where the coefficient J_0 represents the adhesive force between resting AROs. It is a low value, qualitatively reproducing the high contact interactions between unstimulated AROs which, in the absence of external stimulations, tend to remain closely packed in circular islands, as it is possible to appreciate in the representative experimental images in [23, 78].

The above relations reproduce the fact that Met activation induces the disruption of cell-cell adhesion junction by the dispersal of E-cadherin and β-catenin from the intercellular complexes [23]. It is useful to notice that, if we had used the basic CPM, without the compartmentalization technique, it would have been impossible to define a realistic relation of the local cell adhesive strength and the local quantity of activated Met. Moreover, since, obviously, cells cannot break into small fragments, we fix very low bond energies $J_{C,N}^{int}$ and $J_{C,M}^{int}$. For the same reasons of the example in section 3.1.1, the unrealistic contacts between the nucleus and the PM within the same cell and the adhesion energy between the cell PM and the ECM are not considered. Furthermore, we obviously neglect the case of a direct interaction between the nuclei and the cytosolic regions of different cells.

Given the Hamiltonian, the transition probability of a spin flip has the form of (3.26). In particular, we test the model using $p(T(t)) = \tanh(T(t))$. For any cell η, $T_{\eta,\sigma}$, with $\tau(\sigma) = N$, is a low constant positive value that mimics the passive motion of the nucleus of η. If $\tau(\sigma) = \{M, C\}$, then $T_{\eta,\sigma}$ represents instead, as seen, a measure of the real motility of η, which is regulated by the intracellular quantity of the activated Rac and Cdc42 molecules; see also [74]. Adopting again the notation of (3.18) and (3.19), for any ARO η and for $\tau(\sigma) = \{C, M\}$, we now have that

- $\mathbf{s}_{\eta,\sigma}^{T,A}(\mathbf{x},t) = \mathbf{s}_{\eta,\sigma}^{T}(\mathbf{x},t) = (r(\mathbf{x},t), c(\mathbf{x},t));$

- $T_{\eta,\sigma}(\mathbf{s}_{\eta,\sigma}^{T,A}(\mathbf{x},t)) = f_T(\mathbf{s}_{\eta,\sigma}^{T,A}(\mathbf{x},t)) = f_T(r(\mathbf{x},t), c(\mathbf{x},t)) = T_0 \left[\frac{1+c(\eta,t)r(\eta,t)}{1+hc(\eta,t)r(\eta,t)}\right]$, where $r(\eta,t) = \sum_{\mathbf{x}\in\eta} r(\mathbf{x},t)$ and $c(\eta,t) = \sum_{\mathbf{x}\in\eta} c(\mathbf{x},t)$ are the actual total intracellular amounts of, respectively, chemicals Rac and Cdc42 in cell η, and T_0 is the ARO basal motility. As given in Table 4.1, T_0 is a low value, which is qualitatively estimated by observing the negligible basal migratory capacity of the unstimulated cell line, as provided with wound healing assays and time-lapse videorecording techniques in [23]. We use a Michaelis–Menten law to model a dose-dependent enhancement of cell motility driven by the total intracellular level of the G-proteins Rac and Cdc42.

4.2. Molecular-level model. The intracellular HGF/Met-driven pathways on which the model is based are depicted in the scheme in Figure 11. Although simplified, they are consistent with biomolecular experiments presented in [21, 99].

The HGF/SF is uniformly added to the culture, it diffuses in the ECM, where it decays at a constant rate, and it is taken up by ARO cells through Met receptors sited in the membrane compartment. Mathematically, the HGF/SF spatial profile thus satisfies the diffusion equation

$$(4.2) \qquad \frac{\partial H(\mathbf{x},t)}{\partial t} = D_H \nabla^2 H(\mathbf{x},t) - \lambda_H H(\mathbf{x},t) - B(\mathbf{x},t,H(\mathbf{x},t)) + S(\mathbf{x},t),$$

where $H(\mathbf{x}, t)$ denotes the local concentration of the peptide at medium site $\mathbf{x}$ (i.e., $\tau(\sigma(\mathbf{x})) = Q$. The coefficients of diffusivity, D_H, and of degradation, λ_H, are assumed to be homogeneous throughout the simulated Matrigel and have been derived from experimental measurements performed for a recent paper of ours [78]. $S(\mathbf{x}, t)$ describes the addition of the growth factor, at a constant rate ϕ_H outside the cells. The HGF/SF binding and uptake by AROs is defined as $B(\mathbf{x}, t, H(\mathbf{x}, t))$ and is limited to a maximum rate of $\beta_H(t) > 0$ over the external surface of the cells:

$$(4.3) \qquad B(\mathbf{x}, t, H(\mathbf{x}, t)) = \min\{\beta_H(t), zH(\mathbf{x}, t)\},$$

where $\tau(\sigma(\mathbf{x})) = Q$ and $\exists \mathbf{x}' \in \Omega'_{\mathbf{x}} : \tau(\sigma(\mathbf{x}')) = M$ and prefactor z is in units of time. This result is realistic since the capacity of an ARO cell to locally uptake the growth factor through its boundary will saturate at a rate-limit, β_H, which is the maximum number of HGF/SF molecules that can be locally bound and internalized per unit of time. To compute $\beta_H(t)$, we have followed the discussion provided in [7] for the uptake of VEGF molecules by an endothelial cell. In particular, we have here considered a spatially homogeneous average number of Met receptors per cell membrane site; this number has been estimated by dividing the total number of HGF receptors in a generic ARO cell for the actual extension (i.e., at time t) of the membrane of the cell to which the site belongs. Moreover, we have taken into account of an instantaneous HGF/SF-receptor complex internalization rate of $4.3 \cdot 10^{-4}$ per second [31], and 95 kDa as the molecular weight for an HGF/SF molecule [20]. We now define the local number of activated Met receptors:

$$(4.4) \qquad m(\mathbf{x}, t) = \sum_{\mathbf{x}' \in \Omega'_{\mathbf{x}}} z^{-1} B(\mathbf{x}', t, H(\mathbf{x}, t)),$$

where $\tau(\sigma(\mathbf{x})) = M$ and $\tau(\sigma(\mathbf{x}')) = Q$ and z is the same as in (4.3). In (4.4) we have assumed a one-to-one interaction between the HGF/SF molecules and their surface receptors [20]. The activation of Met receptors then initiates a series of events that regulate the cytosololic biochemical kinetics of the PI3K and MAPK molecules:

$$(4.5) \qquad \frac{\partial p(\mathbf{x}, t)}{\partial t} = D_p \nabla^2 p(\mathbf{x}, t) - \lambda_p p(\mathbf{x}, t) + \frac{\mu_p \Upsilon(\mathbf{x}, t)}{\mu_{p,0} + \Upsilon(\mathbf{x}, t)};$$

$$(4.6) \qquad \frac{\partial k(\mathbf{x}, t)}{\partial t} = D_k \nabla^2 k(\mathbf{x}, t) - \lambda_k k(\mathbf{x}, t) + \frac{\mu_k \Upsilon(\mathbf{x}, t)}{\mu_{k,0} + \Upsilon(\mathbf{x}, t)}.$$

The diffusion coefficients, D_p, D_k, and the degradation rates, λ_p, λ_k, of PI3K and MAPK are assumed to be constant and homogeneous within cell cytosol and are taken from theoretical works presented in literature [42, 48, 54]. The third terms in (4.5) and (4.6) describe the PI3K and MAPK production, which is triggered by the Met receptors at the sub-PM region, as

$$(4.7) \qquad \Upsilon(\mathbf{x}, t) = \sum_{\mathbf{x}' \in \Omega'_{\mathbf{x}}} m(\mathbf{x}', t),$$

where $\tau(\sigma(\mathbf{x})) = C$ and $\tau(\sigma(\mathbf{x}')) = M$. In the absence of specific determinations for AROs, the Michaelis–Menten coefficients μ_k and $\mu_{k,0}$ are chosen to reproduce the curve of the HGF/SF-dependent MAPK phosphorylation provided for retinal endothelial cells (RECs) in [12]. μ_p and $\mu_{p,0}$ are estimated to fit the maximal amount

of phosphorylated PI3K at a given concentration of HGF/SF, which has been measured in the same article. Finally, the intracellular quantities of the activated Rac and Cdc42 are regulated, respectively, by the equations

$$(4.8) \qquad \frac{\partial c(\mathbf{x},t)}{\partial t} = D_c \nabla^2 c(\mathbf{x},t) - \lambda_c c(\mathbf{x},t) + \mu_{p-c} p(\mathbf{x},t) + \mu_{k-c} k(\mathbf{x},t),$$

$$(4.9) \quad \frac{\partial r(\mathbf{x},t)}{\partial t} = D_r \nabla^2 r(\mathbf{x},t) - \lambda_r r(\mathbf{x},t) + \mu_{p-r} p(\mathbf{x},t) + \mu_{k-r} k(\mathbf{x},t) + \mu_{c-r} c(\mathbf{x},t),$$

where $\tau(\sigma(\mathbf{x})) = \{C, N\}$ and the diffusion and decay rates are constant. The third and fourth terms in (4.8) describe the activation of Cdc42 mediated by PI3K and MAPK, with constant rates μ_{p-c} and μ_{k-c}. In literature there are no values available for such constants; however, we set $\mu_{p-c} < \mu_{k-c}$ to describe a stronger dependency of Cdc42 on MAPK and a weaker dependency on PI3K. This is biologically consistent as PI3K activates Cdc42 only in a direct way, while MAPK interacts with the G-protein through distinct pathways [87]. The last three analogous terms in (4.9) reproduce the triple regulation, by PI3K, MAPK, and Cdc42, on the activation of Rac at constant rates given by μ_{p-r}, μ_{k-r}, and μ_{c-r}, respectively. Given the value of μ_{c-r} estimated in the case of a moving keratocyte in [53], in the absence of other specific published estimates, we set $\mu_{p-r} = \mu_{k-r} = \mu_{c-r}$.

4.3. Results. The domain Ω is a square lattice of 1500×1500 lattice sites, with periodic boundary conditions. The characteristic length of each grid site is scaled to 0.5 μm, and thus Ω represents a section of a 24-well of size 0.75 mm. One MCS corresponds to 1 s. Diffusion processes are integrated using an explicit Euler method on lattices with the same spatial resolution of Ω, with sufficiently small time steps to guarantee numerical stability (i.e., 10 diffusion steps per MCS). The initial conditions consist of a confluent population of cells scraped by a wound of $d_0 = 600$ pixels (300 μm). The width of the scratch is lower than in experimental cases in order to avoid cell overlapping and to compensate for the absence of mitosis.

As shown in Figure 12(B), without HGF/SF stimulation, the simulated ARO cells barely display any detectable healing after 8 h, which is indicative of their inability to invade the tissue. In particular, they typically maintain close contacts with each other and feature negligible movement. The evolution of the unstimulated ARO culture coincides qualitatively well with experimental evidence, as shown in the same figure and provided in [23]. This gives us confidence in the choice made for the parameters describing the basal properties of the simulated AROs. After the addition of a nanomolar concentration of the chemical, the cell population is instead observed to have an evident enhancement of motility, as the overall migration of the two masses is biased toward the gap. The AROs placed at the fronts have loosened contacts, dissociated, moved from their original site, and started wandering in close proximity, displaying an evident capability to invade open spaces. In other words, they have lost the physiological regulation of the *contact-inhibition* mechanism. Also this behavior is consistent with the relative experimental counterpart; see Figure 12(C) and [23].

As is usual practice in experimental work [67], the healing capability of the population is quantified by the rate of advance of the wound edges (in percentage), which is given by

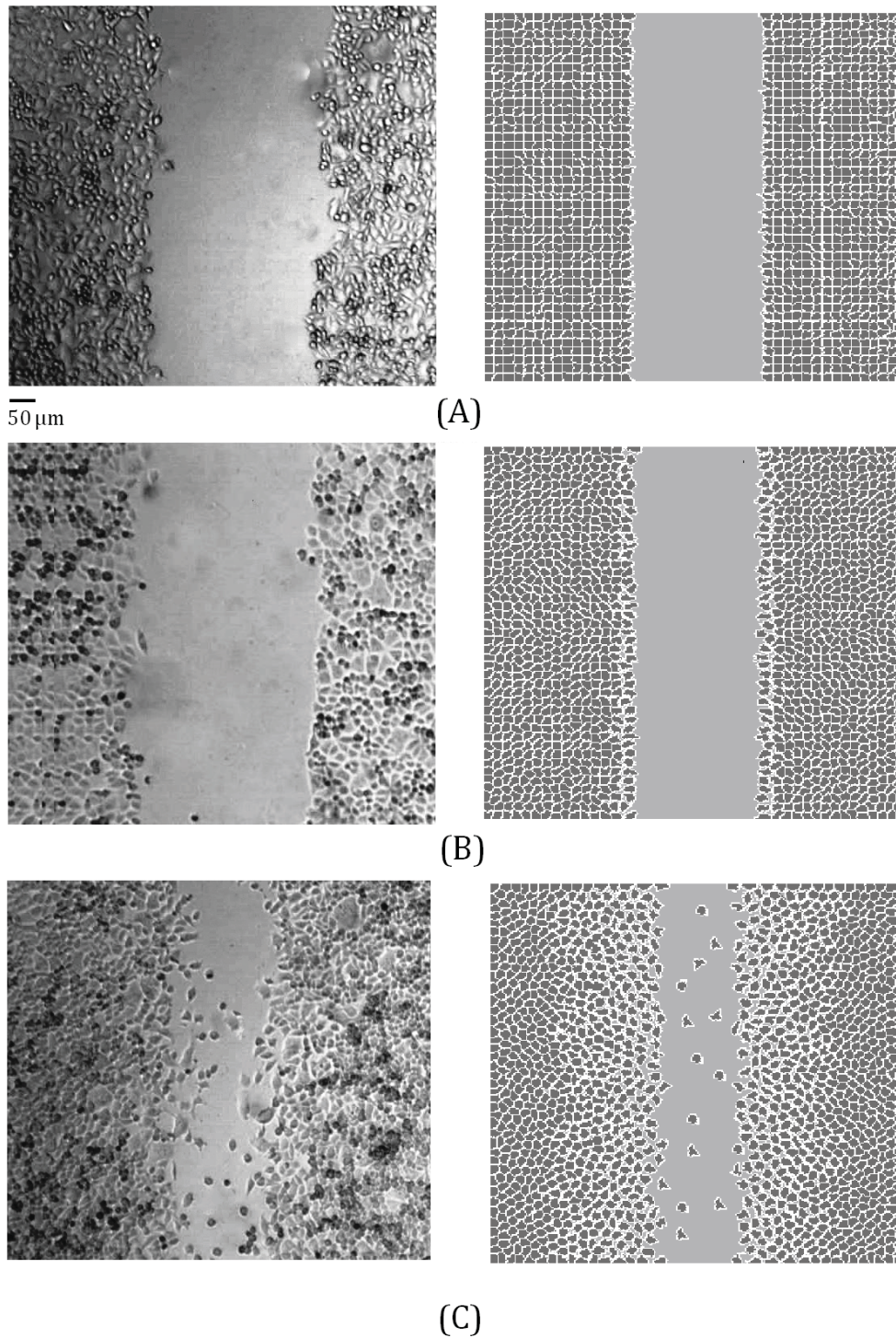$$(4.10) \qquad\qquad D(t) = \frac{1}{N} \sum_{i=1}^{N} \left(1 - \frac{d_i(t)}{d_0}\right) \cdot 100,$$

FIG. 12. *Comparison of the experimental (first column) and simulated (second column) wound healing. The pictures show healing at* (A) $t = 0$ *h and* (B–C) $t = 8$ *h, in the absence of HGF/SF* (B), *and in the presence of HGF/SF* (C).
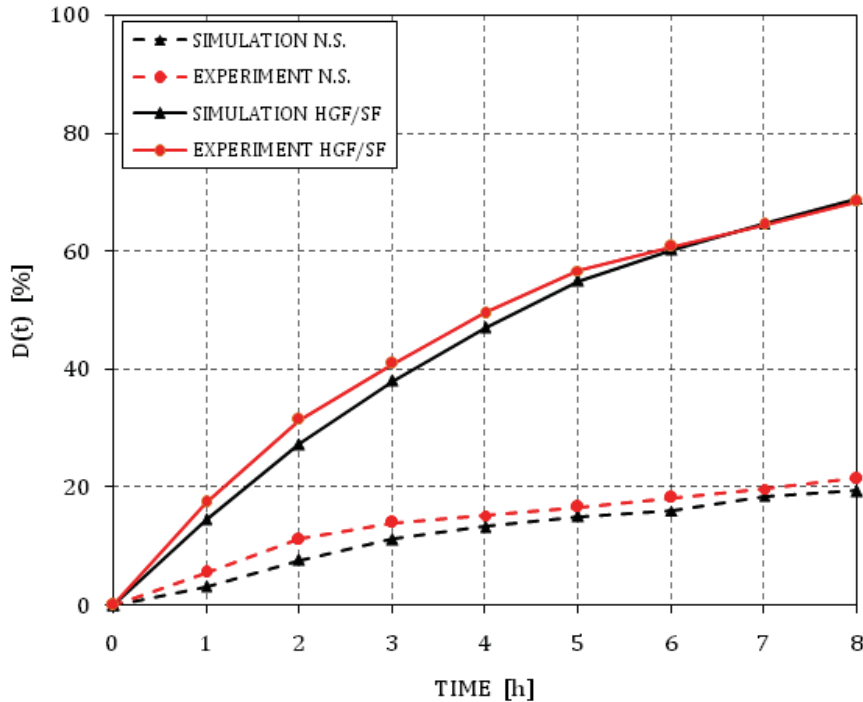
FIG. 13. *Evolution in time of the wound healing process. Comparison between experimental and simulated results in the case of control conditions (no stimulation, dotted lines) and with HGF/SF stimulation (solid lines).*

where d_i represents the distance between a couple of cells across the wound, and d_0 is the initial width of the scratch. The average of $N = 30$ randomly chosen values is used to avoid biases toward accounting for outlier individuals. As shown in Figure 13, the healing of the simulated population, in both control conditions and in the case of HGF/SF treatment, is slightly slower than the experimental one. However, after the initial phase ($t > 2$ h), it evolves at a comparable rate in both cases. Figure 14 offers a definitive confirmation of the HGF-induced increase in cell motility; we compare, in fact, single-cell trajectories obtained by following the displacement of the cell center of mass during the whole healing resulting from the experiments and the numerical simulation. It is worth noticing that in both control conditions and after the HGF/SF treatment, AROs feature an isotropic Brownian movement. This motion can easily be seen from an observation of the circular shape of the delimited area of the chart. Moreover, the increased size of the oval highlights the enhanced migratory capacity of cells in the presence of the growth factor, as the mean effective distance covered by the stimulated individuals is more than doubled (12 μm compared to 5 μm).

5. Computational implementation. The implementation of the CPM core algorithm (i.e., the definition of the Hamiltonian and the modified Metropolis iteration) requires a simple code, which has never created problems for most researchers. CPM users have therefore usually written their own software programs, which were built according the specific application they were developing. However, as mentioned in [6], these proprietary versions were often incompatible, making both the replication of published results almost impossible and the integration of new CPM extensions
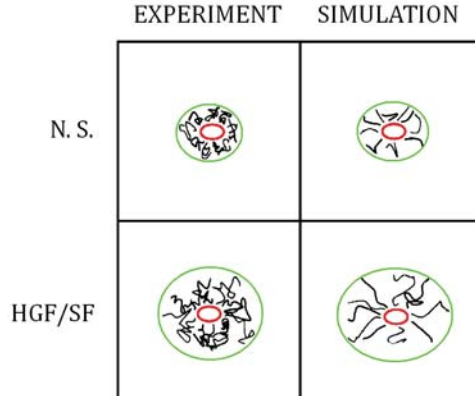
FIG. 14. *HGF/SF-mediated increase in cell motility. Single-cell motion tracks obtained from 8-hour time-lapse experiments and simulations of ARO cells cultured in the presence or absence (N.S.) of HGF (100 U/ml), as indicated. Ten representative tracks were chosen for each experimental condition and optimally arrayed for picture presentation. The red oval positioned at the center of each group of tracks represents the size of a single cell. The green ovals give a measure of the maximum of the effective cell displacements for each condition.*

considerably difficult.

In order to obtain a common CPM-based program, which would have allowed researchers to communicate, combine efforts, and compare and validate their results, several groups have released open-source, extensible packages over the last few years. Among others, the CompuCell3D[1] environment has recently become a standard program for the implementation of basic CPM applications. CC3D was jointly set up by groups at the University of Notre Dame[2] and at the Biocomplexity Institute of Indiana University at Bloomington,[3] and it is still under full and active development. Among its C++ core module, CC3D uses an XML-based markup language and a reasonably simple Python scripting (i.e., plug-ins and stepables) to define the simulated system and to control the model parameters. The resulting simulations are then run from a flexible graphical player.

Our extended CPM has been implemented by a modified version of CC3D. Although the compartmentalization approach was already a standard feature of the program, the other developments have required structural changes. The introduction of the new probability function in (3.26) has led to a modification of the core of the code (i.e., of the part that deals with the basic iteration of the Metropolis algorithm). A group of Python routines, which are set to run within the CC3D framework itself, has instead been implemented for the numerical solution of the models of the individual internal dynamics, as well as for the interfacing of their outcomes with the basic CPM. In principle, these separated microscopic models could also have been approached by adopting external connections between the standard CC3D and some existing packages that deal with biochemical pathways and RD systems (such as BioSpice[4] or Systems Biology Workbench;[5] see [6]. Our choice was done to avoid those

---

[1] http://www.compucell3d.org

[2] http://www.nd.edu

[3] http://www.biocomplexity.indiana.edu

[4] http://www.biospice.org

[5] http://www.sbw.sourceforge.net

compatibility problems that usually arise from the interoperability between different software programs. However, in the free-ware spirit of CC3D and of the other codes that implement the CPM, any interested readers can contact the authors to obtain further information on the program modifications and, if necessary, to get either the entire software or parts of it.

Finally, it is obvious that the improvements in the CPM presented so far require increasing computational power, therefore causing a significant slow down in the speed of the relative simulations. For example, a realization of the wound healing model in section 4 takes almost 4 hours when using a normal notebook, while a simulation of the analogous phenomenon approached with the basic CPM would last less than 30 minutes. To limit this type of issue, we strongly advise researchers to make a preliminary study of the problem of interest and to decide on the needed level of detail. Typically, if the biological phenomenon requires an accurate description of the microscopic scale of individuals, it should also allow one to take into account a small number of individuals themselves. On the contrary, if it requires the simulation of a huge population (for example, a full model of organ morphogenesis requires the simulation of millions of cells), the level of detail for each element can be significantly decreased. In other words, CPM authors should always follow this law:

$$\text{number of simulated individuals} \cdot \text{details of each individual} = \text{constant.}$$

However, it is not always possible to either simplify the internal structure of simulated individuals or to reduce their number. For instance, a full extended CPM of the morphogenesis of a complete organ or of an entire embryo would require the representation of 10^6–10^8 compartmentalized cells, with the relative subcellular dynamics; given that CPM realizations are usually run hundreds of times to average out the results determined by the same values of parameters, the first outcomes might be obtained after months. Efficient computational techniques, able to significantly increase the simulation speed, would therefore be needed. As mentioned in [6, 17], one of the main issues in the CPM implementations is that too low acceptance probabilities of spin flips (i.e., 10^{-4}–10^{-6}) often waste a lot of calculation time. In this regard, implementing into the non–Metropolis Monte Carlo algorithms of rejection free dynamics, such as the *N-fold Way* and the *kinetic Monte Carlo approach*, would be particularly productive [8, 30, 45]. For each time step, they in fact do not consider a trial index copy, which may or may not be accepted, but choose only from among the set of allowed lattice updates (i.e., those that decrease the system energy). Obviously, the net computational gain will depend on the balance between the average number of possible spin flips and the average acceptation rate. The *random-walker* (RW) algorithm instead reduces, but does not eliminate, the rejection rate by selecting as target sites only those belonging to an object boundary [13]. The automatic rejection of nonboundary sites, characteristic of a normal algorithm, is therefore eliminated: however, the increment of the computational speed is appreciable only in the presence of large individuals. However, the most attractive area of improvement in CPM computational implementation is represented by the use of a distribute computing, where the overall simulation domain is divided into equivalent subdomains, which are in turn assigned to different nodes, as addressed again in [6]. A first parallel version of the original Potts method has been implemented in [95] on a model of grain growth, where the effective energy consisted only of local grain boundary interactions, so that each spin flip changed only the energies of its neighbors. Moreover, a recent RW distributing implementation of the CPM ran significantly faster [36]; however,

the proposed parallel scheme required shared memory with all processors sharing the same subdomains. This issue therefore limited the total domain extension to the memory size of a single computer. Indeed, following the useful and detailed explanations provided in [6, 17], the main difficulty in all forms of CPM parallelization is that the effective energy is nonlocal: when a given object crosses between nodes, any modification to it requires an efficient parameter passing between nodes, so that the overall computation does not use stale values. Therefore, naive parallelizations, where the activity of each processor is restricted to a predefined subdomain of the total lattice, will increase the frequency of interprocessor communication for synchronization, and, eventually, the waiting time of each node will be much greater than its calculating time. An interesting attempt to overcome this issue has been made with the *Checkerboard algorithm*, presented in [17]. Its authors have used an improved data structure to describe simulated individuals and have further decomposed the subdomain assigned to each node into smaller subgrids (i.e., sublattices), chosen so that the corresponding ones on different processors do not interact. In this way, an update in one sublattice affects only the set of the nearest-neighbor sublattices. Each node is therefore able to determine the spin flips affecting neighbor nodes, to accumulate them, and to pass them synchronously. In this case, the speed gain increases with the size of the subgrids per processor and decreases with the interaction range. Such a basic checkerboard parallelization can also implement rejection-free or RW methods by using either equivalent or master-slave computations [6].

6. Conclusions. Over the last decade, the CPM method has become a standard technique for cell-to-tissue level in silico biology, first replicating, then guiding, in vitro experiments and eventually leading to new experimental discoveries [33, 52, 59]. In this work, we have offered a brief overview of its biophysical bases and discussed its main limitations. We have also introduced several possible developments and improvements.

First, we have proposed a more realistic representation of biological individuals, based on a compartmentalized approach. Such a technique is not entirely new in CPM applications, but we have applied it in a novel way, using sets of individual compartments with a direct correspondence to their "natural" counterparts, instead of sets of compartments with no biological basis. Among others, of particular relevance is the application of this procedure to represents cells, which can be accurately differentiated into their characteristic subcellular elements, such as the PM, the nucleus, and the cytosol.

Moreover, we have focused on the explicit representation of the internal state of the simulated individuals and on its influence on their phenomenology. Our main assumption has been that the microscopic dynamics within each element mediate its biophysical properties, which, in turn, drive its behavior. Therefore, we have used the classic Potts parameters to interface continuous models reproducing the molecular evolution of the individuals with the mesoscopic CPM describing their phenomenology. The combined use of this multilevel approach with the compartmentalization technique is a further step toward an improved realism of the CPM. It, in fact, allows an accurate localization of microscopic processes within well-characterized internal regions of the simulated individuals (e.g., expression and internalization of receptors at cell membrane, actin polymerization within the cytosol, protein absorption, and activation of signaling cascades in the nucleus). The resulting framework therefore features a complex, but realistic, web of interactions between different submodels focused on different scales and has the potential to accurately describe multiple phenomena

with increased biological usefulness and predictive power.

The third development concerns the introduction of a new family of Boltzmann-like transition probability functions, which better represent the migratory ability (or mobility) of biological elements. In particular, the proposed laws realistically take into account the intrinsic motility of moving individuals, even in the case of energetic favorable displacement attempts.

However, since a powerful modeling approach should be able to adapt to different biological contexts of interest and to represent multiple types of phenomena, we have illustrated some relevant sample simulations. In particular, we have modeled the chemotactic migration of an endothelial cell in both an isotropic undifferentiated medium and in a two-component substrate, and a typical wound healing assay of an ARO cell population stimulated by saturating levels of HGF/SF. In all these cases, the results obtained by the model have agreed with the published experimental observations, thus showing the consistency of our CPM extensions. However, it would also be very useful to test our extended model on other biological problems, some of which have been suggested in the text.

Although our approach has increased the accuracy of CPM applications, it is still not able to deal with many biological details and could obviously be improved in several ways. A first, natural development of the method would be a better characterization of the motion of the individual internal compartments, such as the nucleus in the case of compartmentalized cells. In the present version, in fact, they move almost passively, dragged by displacements of their surrounding regions (i.e., the cytoplasm for the nucleus). In the future, we plan to introduce the possibility of "autonomous" fluctuations of such internal units, which can be independent of the movement of the entire individual they belong to. In our opinion, a further fundamental aspect still to be developed in CPMs is the addition of the genetic level; see also [59]. In this way, it would be possible to analyze the influence of gene network dynamics on the internal state of biological elements and, consequently, on their behavior. In particular, efforts could be made to link the alterations of an individual phenotype to a specific genetic defect.

REFERENCES

[1] M. S. Alber, M. A. Kiskowski, J. A. Glazier, and Y. Jiang, *On cellular automation approaches to modeling biological cells*, in Mathematical Systems Theory in Biology, Communication and Finance, J. Rosenthal and D. S. Gilliam, eds., Springer-Verlag, New York, 2004, pp. 1–40.

[2] B. Alberts, D. Bray, J. Lewis, M. Raff, K. Roberts, and J. D. Watson, *Molecular Biology of the Cell*, 3rd ed., Garland Science, New York, 1994.

[3] A. R. A. Anderson, M. A. J. Chaplain, and K. A. Rejniak, eds., *Single-Cell-Based Models in Biology and Medicine*, Mathematics and Biosciences in Interactions, Birkhäuser, Basel, 2007.

[4] P. B. Armstrong and D. Parenti, *Cell sorting in the presence of cytochalasin b*, J. Cell Biol., 55 (1972), pp. 542–553.

[5] D. Baird, Q. Feng, and R. A. Cerione, *The Cool-2/alpha-Pix protein mediates a Cdc42-Rac signaling cascade*, Curr. Biol., 15 (2005), pp. 1–10.

[6] A. Balter, R. M. H. Merks, N. J. Poplawski, M. Swat, and J. A. Glazier, *The Glazier-Graner-Hogeweg model: Extensions, future directions, and opportunities for further study*, in Single-Cell-Based Models in Biology and Medicine, Mathematics and Biosciences in Interactions, A. R. A. Anderson et al., eds., Birkhäuser, Basel, 2007, pp. 151–167.

[7] A. L. Bauer, T. L. Jackson, and Y. Jiang, *A cell-based model exhibiting branching and anastomosis during tumor-induced angiogenesis*, Biophys. J., 92 (2007), pp. 3105–3121.

[8] A. B. Bortz, M. H. Kalos, and J. L. Lebowitz, *A new algorithm for Monte Carlo simulation of Ising spin systems*, J. Comput. Phys., 17 (1975), pp. 10–18.

[9] T. Bosse, J. Ehinger, A. Czuchra, S. Benesch, A. Steffen, X. Wu, K. Schloen, H. H. Niemann, G. Scita, T. E. B. Stradal, C. Brakebusch, and K. Rottner, *Cdc42 and PI3K drive Rac-mediated actin polymerization downstream of c-Met in distinct and common pathways*, Mol. Cell. Biol., 27 (2007), pp. 6615–6628.

[10] V. Brinkmann, H. Foroutan, H. Sachs, K. M. Weidner, and W. Birchmeier, *Hepatocyte growth factor/scatter factor induces a variety of tissue specific morphogenic programs in epithelial cells*, J. Cell Biol., 131 (1995), pp. 1573–1586.

[11] H. M. Byrne, M. R. Owen, T. Alarcon, J. Murphy, and P. K. Maini, *Modelling the response of vascular tumours to chemotherapy: A multiscale approach*, Math. Models Methods Appl. Sci., 16 (2006), pp. 1219–1241.

[12] W. Cai, S. L. Rook, Z. Y. Jiang, N. Takahara, and L. P. Aiello, *Mechanisms of hepatocyte growth factor–induced retinal endothelial cell migration and growth*, Investigative Ophthalmology and Visual Science, 41 (2000), pp. 1885–1893.

[13] F. P. Cercato, J. C. M. Mombach, and G. G. H. Cavalheiro, *High performance simulations of the Cellular Potts model*, in Proceedings of the 20th International Symposium on High-Performance Computing in an Advanced Collaborative Environment, IEEE, Washington, DC, 2006, p. 28.

[14] R. Chaturvedi, C. Huang, J. A. Izaguirre, S. A. Newman, J. A. Glazier, and M. S. Alber, *A hybrid discrete-continuum model for 3-D skeletogenesis of the vertebrate limb*, in Cellular Automata, Lecture Notes in Comput. Sci. 3305, Springer, New York, 2004, pp. 543–552.

[15] R. Chaturvedi, C. Huang, B. Kazmierczak, T. Schneider, J. A. Izaguirre, T. Glimm, H. G. Hentschel, J. A. Glazier, S. A. Newman, and M. S. Alber, *On multiscale approaches to three-dimensional modelling of morphogenesis*, J. R. Soc. Interface, 2 (2005), pp. 237–253.

[16] A. Chauviere, L. Preziosi, and C. Verdier, eds., *Cell Mechanics: From Single Scaled-Based Models to Multiscale Modeling*, Mathematical and Computational Biology Series, CRC Press, Boca Raton, FL, 2010.

[17] N. Chen, J. A. Glazier, J. A. Izaguirre, and M. S. Alber, *A parallel implementation of the cellular Potts model for simulation of cell-based morphogenesis*, Comput. Phys. Commun., 176 (2007), pp. 670–681.

[18] T. Cickovski, C. Huang, R. Chaturvedi, T. Glimm, H. G. E. Hentschel, M. S. Alber, J. A. Glazier, S. A. Newman, and J. A. Izaguirre, *A framework for three-dimensional simulation of morphogenesis*, IEEE/ACM Trans. Comput. Biol. Bioinform., 2 (2005), pp. 273–288.

[19] B. A. Cipra, *An introduction to the Ising-model*, Amer. Math. Monthly, 94 (1987), pp. 937–959.

[20] P. M. Comoglio and C. Boccaccio, *Scatter factors and invasive growth*, Semin. Cancer Biol., 11 (2000), pp. 153–165.

[21] P. M. Comoglio and M. C. Stella, *HGF: A multifunctional growth factor controlling cell scattering*, Int. J. Biochem. Cell Biol., 31 (1999), pp. 1357–1362.

[22] D. Dan, C. Mueller, K. Chen, and J. A. Glazier, *Solving the advection-diffusion equations in biological contexts using the cellular Potts model*, Phys. Rev. E Stat. Nonlin. Soft Matter Phys., 72 (2005), 041909.

[23] A. De Luca, N. Arena, L. M. Sena, and E. Medico, *Met overexpression confers HGF-dependent invasive phenotype to human thyroid carcinoma cells in vitro*, J. Cell. Physiol., 180 (1999), pp. 365–371.

[24] M. F. Di Renzo, M. Oliviero, R. P. Narsimhan, S. Bretti, S. Giordano, E. Medico, P. Gaglia, P. Zara, and P. M. Comoglio, *Expression of the Met/HGF receptor in normal and neoplastic human tissues*, Oncogene, 6 (1991), pp. 1997–2003.

[25] D. Drasdo and S. Hohme, *Individual-based approaches to birth and death in avascular tumors*, Math. Comput. Modelling, 37 (2003), pp. 1163–1175.

[26] D. Drasdo, *On selected individual-based approaches to the dynamics of multicellular systems*, in Multiscale Modeling, W. Alt and M. Griebel, eds., Birkhäuser, Basel, 2005, pp. 169–203.

[27] D. Drasdo and G. Forgacs, *Modeling the interplay of generic and genetic mechanisms in cleavage, blastulation, and gastrulation*, Dev. Dyn., 219 (2000), pp. 182–191.

[28] C. J. Drake, A. LaRue, N. Ferrara, and C. D. Little, *VEGF regulates cell behavior during vasculogenesis*, Dev. Biol., 224 (2000), pp. 178–188.

[29] S. Etienne-Manneville, *Cdc42—the centre of polarity*, J. Cell Sci., 117 (2004), pp. 1291–1300.

[30] K. A. FICHTHORN AND W. H. WEINBERG, *Theoretical foundations of dynamical Monte Carlo simulations*, J. Chem. Phys., 95 (1991), pp. 1090–1096.

[31] F. M. GABHANN AND A. S. POPEL, *Model of competitive binding of vascular endothelial growth factor and placental growth factor to VEGF receptors on endothelial cells*, Am. J. Physiol. Heart Circ. Physiol., 286 (2004), pp. H153–H164.

[32] C. GIVERSO, M. SCIANNA, L. PREZIOSI, N. LO BUONO, AND A. FUNARO, *Individual cell-based model for in-vitro mesothelial invasion of ovarian cancer*, Math. Model. Nat. Phenom., 5 (2010), pp. 203–223.

[33] J. A. GLAZIER, A. BALTER, AND N. J. POPLAWSKI, *Magnetization to morphogenesis: A brief history of the Glazier-Graner-Hogeweg model*, in Single-Cell-Based Models in Biology and Medicine, Mathematics and Biosciences in Interactions, A. R. A. Anderson, M. A. J. Chaplain, and K. A. Rejniak, eds., Birkhäuser, Basel, 2007, pp. 79–106.

[34] J. A. GLAZIER AND F. GRANER, *Simulation of the differential adhesion driven rearrangement of biological cells*, Phys. Rev. E Stat. Phys. Plasmas Fluids Relat. Interdiscip. Topics, 47 (1993), pp. 2128–2154.

[35] F. GRANER AND J. A. GLAZIER, *Simulation of biological cell sorting using a two dimensional extended Potts model*, Phys. Rev. Lett., 69 (1992), pp. 2013–2017.

[36] E. GUSATTO, J. C. M. MOMBACH, F. P. CERCATO, AND G. H. CAVALHEIRO, *An efficient parallel algorithm to evolve simulations of the cellular Potts model*, Parallel Process. Lett., 15 (2005), pp. 199–208.

[37] H. G. E. HENTSCHEL, T. GLIMM, J. A. GLAZIER, AND S. A. NEWMAN, *Dynamical mechanisms for skeletal pattern formation in the vertebrate limb*, Proc. Biol. Sci., 271 (2004), pp. 1713–1722.

[38] H. N. HIGGS AND T. D. POLLARD, *Activation by Cdc42 and PIP2 of Wiskott-Aldrich syndrome protein (WASp) stimulates actin nucleation by Arp2/3 complex*, J. Cell Biol., 150 (2000), pp. 1311–1320.

[39] P. HOGEWEG, *Evolving mechanisms of morphogenesis: On the interplay between differential adhesion and cell differentiation*, J. Theoret. Biol., 203 (2000), pp. 317–333.

[40] J. HOWARD, *Mechanics of Motor Proteins and the Cytoskeleton*, Sinauer Associates, Sunderland, MA, 2001.

[41] Y. JIANG, *Cellular Pattern Formation*, Ph.D. thesis, University of Notre Dame, South Bend, IN, 2004.

[42] B. N. KHOLODENKO, *Four-dimensional organization of protein kinase signaling cascades: The roles of diffusion, endocytosis and molecular motors*, J. Exp. Biol., 206 (2003), pp. 2073–2082.

[43] E. ISING, *Beitrag zur theorie des ferromagnetismus*, Z. Physik, 31 (1925), p. 253.

[44] N. LAHAT, M. SHEINFELD, E. SOBEL, A. KINARTY, AND Z. KRAIEM, *Divergent effects of cytokines on human leukocyte antigen-DR antigen expression of neoplastic and non-neoplastic human thyroid cells*, Cancer, 69 (1992), pp. 1799–1807.

[45] K.-C. LEE, *Rejection-free Monte Carlo technique*, J. Phys. A, 28 (1995), p. 4835.

[46] E. LESKO AND M. MAJKA, *The biological role of HGF- MET axis in tumor growth and development of metastasis*, Front. Biosci., 13 (2008), pp. 1271–1280.

[47] J. S. LOWENGRUB, H. B. FRIEBOES, F. JIN, Y.-L. CHUANG, X. LI, P. MACKLIN, S. M. WISE, AND V. CRISTINI, *Nonlinear modelling of cancer: Bridging the gap between cells and tumours*, Nonlinearity, 23 (2010), pp. R1–R91.

[48] L. MA, C. JANETOPOULOS, L. YANG, P. N. DEVREOTES, AND P. A. IGLESIAS, *Two complementary, local excitation, global inhibition mechanisms acting in parallel can explain the chemoattractant-induced regulation of PI(3,4,5)P3 response in Dictyostelium cells*, Biophys. J., 87 (2004), pp. 3764–3774.

[49] A. W. MAHONEY, B. G. SMITH, N. S. FLANN, AND G. J. PODGORSKI, *Discovering novel cancer therapies: A computational modeling and search approach*, in IEEE Conference on Computational Intelligence in Bioinformatics and Bioengineering, IEEE, Washington, DC, 2008, pp. 233–240.

[50] P. K. MAINI, L. OLSEN, AND J. A. SHERRATT, *Mathematical models for cell-matrix interactions during dermal wound healing*, Internat. J. Bifur. Chaos Appl. Sci. Engrg., 12 (2008), pp. 2021–2029.

[51] A. F. M. MARÉE, V. A. GRIENEISEN, AND P. HOGEWEG, *The cellular Potts model and biophysical properties of cells, tissues and morphogenesis*, in Single-Cell-Based Models in Biology and Medicine, Mathematics and Biosciences in Interactions, A. R. A. Anderson, M. A. J. Chaplain, and K. A. Rejniak, eds., Birkhäuser, Basel, 2007, pp. 107–136.

[52] A. F. M. MARÉE AND P. HOGEWEG, *How amoeboids self-organize into a fruiting body: Multicellular coordination in Dictyostelium discoideum*, Proc. Natl. Acad. Sci. USA, 98 (2001),

pp. 3879–3883.

[53] A. F. M. Marée, A. Jilkine, A. Dawes, V. A. Grieneisen, and L. Edelstein-Keshet, *Polarization and movement of keratocytes: A multiscale modelling approach*, Bull. Math. Biol., 68 (2006), pp. 1169–1211.

[54] N. I. Markevich, M. A. Tsyganov, J. B. Hoek, and B. N. Kholodenko, *Long-range signaling by phosphoprotein waves arising from bistability in protein kinase cascades*, Mol. Sys. Biol., 2 (2006), 61.

[55] A. M. Mongiovi, J. Huff, M. A. Jelinek, A. Follenzi, G. Gaudino, J. T. Parsons, P. M. Comoglio, and E. Medico, *The tyrosine kinase receptors Ron and Sea control "scattering" and morphogenesis of liver progenitor cells in vitro*, Mol. Biol. Cell, 7 (1996), pp. 495–504.

[56] R. M. H. Merks and J. A. Glazier, *Dynamic mechanisms of blood vessel growth*, Nonlinearity, 19 (2006), pp. C1–C10.

[57] R. M. H. Merks, S. V. Brodsky, M. S. Goligorksy, S. A. Newman, and J. A. Glazier, *Cell elongation is key to in silico replication of in vitro vasculogenesis and subsequent remodeling*, Dev. Biol., 289 (2006), pp. 44–54.

[58] R. M. H. Merks, E. D. Perryn, A. Shirinifard, and J. A. Glazier, *Contact-inhibited chemotactic motility: Role in de novo and sprouting blood vessel growth*, PLoS Comput. Biol., 4 (2008), e1000163.

[59] R. M. H. Merks and P. Koolwijk, *Modeling morphogenesis in silico and in vitro: Towards quantitative, predictive, cell-based modeling*, Math. Model. Nat. Phenom., 4 (2009), pp. 149–171.

[60] N. Metropolis, A. Rosenbluth, M. N. Rosenbluth, A. H. Teller, and E. Teller, *Equation of state calculations by fast computing machines*, J. Chem. Phys., 21 (1953), pp. 1087–1092.

[61] A. Mochizuki, *Pattern formation of the cone mosaic in the zebrafish retina: A cell rearrangement model*, J. Theoret. Biol., 215 (2002), pp. 345–361.

[62] J. C. M. Mombach and J. A. Glazier, *Single cell motion in aggregates of embryonic cells*, Phys. Rev. Lett., 76 (1996), pp. 3032–3035.

[63] J. C. M. Mombach, R. M. C. De Almeida, G. L. Thomas, A. Upadhyaya, and J. A. Glazier, *Bursts and cavity formation in Hydra cells aggregates: Experiments and simulations*, Phys. A, 297 (2001), pp. 495–508.

[64] J. C. M. Mombach, R. M. C. De Almeida, and G. L. Iglesias, *Mitosis and growth in biological tissues*, Phys. Rev. E Stat. Phys. Plasmas Fluids Relat. Interdiscip. Topics, 48 (1993), pp. 598–608.

[65] J. Moreira and A. Deutsch, *Pigment pattern formation in zebrafish during late larval stages: A model based on local interactions*, Develop. Dynam., 232 (2005), pp. 33–42.

[66] N. B. Ouchi, J. A. Glazier, J. P. Rieu, A. Upadhyaya, and J. Sawada, *Improving the realism of the cellular Potts model in simulations of biological cells*, Phys. A, 329 (2003), pp. 451–458.

[67] R. Pedeux, D. Ythier, and A. Duperray, *Cell motility and tumor suppressor genes*, in Cell Mechanics: From Single Scale-Based Models to Multiscale Modeling, Mathematical and Computational Biology Series, A. Chauvier, L. Preziosi, and C. Verdier, eds., CRC Press, Boca Raton, FL, 2010, pp. 67–88.

[68] T. D. Pollard and G. G. Borisy, *Cellular motility driven by assembly and disassembly of actin filaments*, Cell, 112 (2003), pp. 453–465.

[69] N. J. Poplawski, A. Shirinifard, M. Swat, and J. A. Glazier, *Simulation of single–species bacterical–biofilm growth using the Glazier–Graner–Hogeweg model and the CompuCell3D modeling environment*, Math. Biosci. Eng., 5 (2008), pp. 355–388.

[70] N. J. Poplawski, M. Swat, J. S. Gens, and J. A. Glazier, *Adhesion between cells, diffusion of growth factors, and elasticity of the AER produce the paddle shape of the chick limb*, Phys. A, 373 (2007), pp. 521–532.

[71] R. B. Potts, *Some generalized order-disorder transformations*, Proc. Cambridge Phil. Soc., 48 (1952), pp. 106–109.

[72] S. M. Rafelski and J. A. Theriot, *Crawling toward a unified model of cell motility: Spatial and temporal regulation of actin dynamics*, Annu. Rev. Biochem., 73 (2004), pp. 209–239.

[73] A. J. Ridley, H. F. Paterson, C. L. Johnston, D. Diekmann, and A. Hall, *The small GTP-binding protein Rac regulates growth factor-induced membrane ruffling*, Cell, 70 (1992), pp. 401–410.

[74] A. J. Ridley, *Rho GTPases and cell migration*, J. Cell Sci., 114 (2001), pp. 2713–2722.

[75] B. M. Rubenstein and L. J. Kaufman, *The role of extracellular matrix in glioma invasion: A cellular Potts model approach*, Biophys. J., 95 (2008), pp. 5661–5680.

[76] N. J. SAVILL AND P. HOGEWEG, *Modelling morphogenesis: From single cells to crawling slugs*, J. Theoret. Biol., 184 (1997), pp. 118–124.

[77] N. J. SAVILL AND J. A. SHERRATT, *Control of epidermal stem cell clusters by Notch-mediated lateral induction*, Dev. Biol., 258 (2003), pp. 141–153.

[78] M. SCIANNA, R. M. H. MERKS, L. PREZIOSI, AND E. MEDICO, *Individual cell-based models of cell scatter of ARO and MLP-29 cells in response to hepatocyte growth factor*, J. Theoret. Biol., 260 (2009), pp. 151–160.

[79] M. SCIANNA, *A multiscale hybrid model for pro-angiogenic calcium signals in a vascular endothelial cell*, Bull. Math. Biol., to appear.

[80] M. SCIANNA, L. MUNARON, AND L. PREZIOSI, *A multiscale hybrid approach for vasculogenesis and related potential blocking therapies*, Prog. Biophys. Mol. Biol., 106 (2011), pp. 450–462.

[81] G. SERINI, D. AMBROSI, E. GIRAUDO, A. GAMBA, L. PREZIOSI, AND F. BUSSOLINO, *Modeling the early stages of vascular network assembly*, EMBO J., 22 (2003), pp. 1771–1779.

[82] A. SHIRINIFARD, J. S. GENS, B. L. ZAITLEN, N. J. POPLAWSKI, M. SWAT, AND J. A. GLAZIER, *3D multi-cell simulation of tumor growth and angiogenesis*, PLoS ONE, 4 (2009), e7190.

[83] J. STARRUSS, T. BLEY, L. SØGAARD-ANDERSEN, AND A. DEUTSCH, *A new mechanism for collective migration in Myxococcus Xanthus*, J. Stat. Phys., 128 (2007), pp. 269–286.

[84] M. S. STEINBERG, *Reconstruction of tissues by dissociated cells. Some morphogenetic tissue movements and the sorting out of embryonic cells may have a common explanation*, Science, 141 (1963), pp. 401–408.

[85] M. S. STEINBERG, *Does differential adhesion govern self-assembly processes in histogenesis? Equilibrium configurations and the emergence of a hierarchy among populations of embryonic cells*, J. Exp. Zool., 173 (1970), pp. 395–433.

[86] M. STOKER, E. GHERARDI, M. PERRYMAN, AND J. GRAY, *Scatter factor is a fibroblast-derived modulator of epithelial cell mobility*, Nature, 21 (1987), pp. 239–242.

[87] K. SZCZUR, H. XU, S. ATKINSON, Y. ZHENG, AND M.-D. FILIPPI, *Rho GTPase CDC42 regulates directionality and random movement via distinct MAPK pathways in neutrophils*, Blood, 108 (2006), pp. 4205–4213.

[88] L. TAMAGNONE AND P. M. COMOGLIO, *Control of invasive growth by hepatocyte growth factor (HGF) and related scatter factors*, Cytokine Growth Factor Rev., 8 (1997), pp. 129–142.

[89] C. TOMATIS, A. FIORIO PLA, AND L. MUNARON, *Cytosolic calcium microdomains by arachidonic acid and nitric oxide in endothelial cells*, Cell Calcium, 41 (2007), pp. 261–269.

[90] L. TRUSOLINO AND P. M. COMOGLIO, *Scatter-factor and semaphorin receptors: Cell signalling for invasive growth*, Nat. Rev. Cancer, 2 (2002), pp. 289–300.

[91] S. TURNER AND J. A. SHERRATT, *Intercellular adhesion and cancer invasion: A discrete simulation using the extended Potts model*, J. Theoret. Biol., 216 (2002), pp. 85–100.

[92] T. WALTHER, H. REINSCH, A. GROSSE, K. OSTERMANN, A. DEUTSCH, AND T. BLEY, *Mathematical modeling of regulatory mechanisms in yeast colony development*, J. Theoret. Biol., 229 (2004), pp. 327–338.

[93] N. WANG, J. D. TYTELL, AND D. E. INGBER, *Mechanotransduction at a distance: Mechanically coupling the extracellular matrix with the nucleus*, Nat. Rev. Mol. Cell Biol., 10 (2009), pp. 75–82.

[94] K. M. WEIDNER, J. BEHRENS, J. VANDEKERCKHOVE, AND W. BIRCHMEIER, *Scatter factor: Molecular characteristics and effect on the invasiveness of epithelial cells*, J. Cell Biol., 111 (1990), pp. 2097–2108.

[95] S. A. WRIGHT, S. J. PLIMPTON, T. P. SWILER, R. M. FYE, M. F. YOUNG, AND E. A. HOLM, *Potts-model grain growth simulations: Parallel algorithms and applications*, SAND Report 97-1925, Sandia National Laboratories, Albuquerque, NM, 1997.

[96] Z. XU, J. LIOI, J. MU, M. M. KAMOCKA, X. LIU, D. Z. CHEN, E. D. ROSEN, AND M. S. ALBER, *A multiscale model of venous thrombus formation with surface-mediated control of blood coagulation cascade*, Biophys. J., 98 (2010), pp. 1723–1732.

[97] Z. XU, N. CHEN, S. SHADDEN, J. E. MARSDEN, M. KAMOCKA, E. D. ROSEN, AND M. S. ALBER, *Study of blood flow impact on growth of thrombi using a multiscale model*, Soft Matter, 5 (2009), pp. 769–779.

[98] Z. XU, N. CHEN, M. M. KAMOCKA, E. D. ROSEN, AND M. S. ALBER, *A multiscale model of thrombus development*, J. R. Soc. Interface, 5 (2008), pp. 705–722.

[99] Y. ZHANG AND G. F. VANDE WOUDE, *HGF/SF-Met signaling in the control of branching morphogenesis and invasion*, J. Cell. Biochem., 88 (2003), pp. 408–417.

[100] V. P. ZHDANOV AND B. KASEMO, *Simulation of the growth and differentiation of stem cells on a heterogeneous scaffold*, Phys. Chem. Chem. Phys., 6 (2004), pp. 4347–4350.